Chapter 14

Wing Scans: Data Reduction and Pinhole Effective Areas

Terrance J. Gaetz

In this chapter we discuss the data taken for the wing scan experiments at XRCF; in the next chapter the data are analyzed to extract information about the mirror surfaces. In the encircled energy experiments (see Chapter 16), the energy passing within concentric pinholes from 10 μm diameter up to 35 mm diameter was measured. The wing scans provide information on the PSF wings in some directions out to 105 mm from the image core. The wing scan experiment was designed to map out the far wings of the Point Spread Function, or PSF, at angles $\gtrsim$1 mm (about $20''$ away from the core). Because of time constraints, only a selected portions of the wings could be mapped in detail. This was accomplished by a series of horizontal (Y) or vertical (Z) pinhole scans through the PSF. The pinhole diameters were 1, 4, 10, 20, and 35 mm; the scan was centered on the core of the PSF, and up to 3 points were sampled to either side (*i.e.*, $-3D_{ap}$, $-2D_{ap}$, $-1D_{ap}$, 0, $+1D_{ap}$, $+2D_{ap}$, $+3D_{ap}$).

The quadrant shutters were used to isolate quadrants of individual mirror pairs; see Chapter C for a description of the quadrant shutter nomenclature. Wing scans were performed at various energies for each quadrant of each mirror pair. The combinations of quadrant, energy, and pinhole diameter for the single quadrant wing scans are given in Table 14.3. In addition, a small number of double-quadrant wing scans were performed. In these scans, opposing quadrants for a given shell were open and the HRMA was at zero pitch and yaw; because of the presumed symmetry of the HRMA, data were taken only for points to one side of the HRMA ($+D_{ap}$, $+2D_{ap}$, and $+3D_{ap}$ for a given aperture diameter D_{ap}). Because of problems with shutters sticking, the 4N4S and 6N6S scans were performed with shutter 3B also open (*i.e.*, they were really 4N4S3B and 6N6S3B scans). In order to correct for this, additional 3B Z-scans were performed for the 1 mm and 4 mm pinholes only. These pinhole measurements are listed in Table 14.2.

The far wings of the PSF result mainly from scattering by the optic surfaces, primarily scattering from microroughness. In principle dust scattering could also contribute but any dust component was expected to be small because of the cleanliness of the AXAF optics. For grazing incidence reflection, scattering by microroughness is predominantly in-plane with only a small out-of-plane component. Consequently, Y-scans were performed for the North and South quadrants, while Z-scans were used for the Top and Bottom quadrants; a Y-scan was also performed at C-Kα for the shell 6 bottom quadrant in order to look for out-of-plane scattering resulting from any dust contamination. In addition, a very small number of Y-scans were performed at Al-Kα for the shell 3 bottom quadrant.

Table 14.1: XRCF Single Quadrant Wing Scan Measurements (by shell)

Energy (keV)	diam (mm)	T1	N1	B1	S1	T3	N3	B3	S3	T4	N4	B4	S4	T6	N6	B6	S6
0.277	1															○	
0.277	4															○	
0.277	10															○	
0.277	20															○	
0.277	35																
1.486	1	○	○	○	○	○	○	○	○	○	○	○	○	○	○	○	○
1.486	4	○	○	○	○	○	○	○	○	○	○	○	○	○	○	○	○
1.486	10	○	○	○	○		○		○		○		○		○		○
1.486	20	○	○	○	○	○	○	○	○	○	○	○	○	○	○	○	○
1.486	35		○		○		○		○		○		○		○		○
4.51	1	○	○	○	○				○				○				○
4.51	4	○	○	○	○				○				○				○
4.51	10	○	○	○	○				○				○				○
4.51	20	○	○	○	○				○				○				○
4.51	35		○		○				○				○				○
5.41	1								○				○				○
5.41	4								○				○				○
5.41	10								○				○				○
5.41	20								○				○				○
5.41	35								○				○				○
6.4	1					○	○	○	○	○	○	○	○	○	○	○	○
6.4	4					○	○	○	○	○	○	○	○	○	○	○	○
6.4	10					○	○	○	○	○	○	○	○	○	○	○	○
6.4	20					○	○	○	○	○	○	○	○	○	○	○	○
6.4	35						○				○		○		○		○
8.03	1												○	○	○[†]	○	○
8.03	4												○	○	○[†]	○	○
8.03	10												○	○	○[†]	○	○
8.03	20												○	○	○[†]	○	○
8.03	35												○		○[†]		○

[†]CMBD indicates yaw = $-1.88'$; other logs indicate that yaw = $+1.88'$ was actually used.

In order to expose as much of the optic as is possible given the finite source distance at XRCF, the tests were done one quadrant at a time with the mirror assembly pitched or yawed a few minutes of arc so that the diverging rays from the source would strike the mirror approximately parallel to the mirror assembly axis of rotational symmetry (closer to on-orbit, infinite source distance conditions). Nominally, the pitch or yaw should have been $3.56'$, $2.87'$, $2.53'$, or $1.88'$ for shells 1, 3, 4, and 6, respectively. Because of confusion about the orientation of the optical axis relative to the facility axis, some yaw offsets were in reality about 1 arcmin away from the intended value; the actual pitch/yaw combinations are given in Table 14.3 below.

In one case (shell 6N at Cu-Kα, the CMDB indicates a requested yaw of $-1.88'$ instead of the

Table 14.2: XRCF Double Quadrant Wing Scan Measurements

Energy (keV)	diam (mm)	4N4S3B	6N6S3B	3B
1.486	1	∘	∘	∘
1.486	4	∘	∘	∘
1.486	10	∘	∘	
1.486	20	∘	∘	
1.486	35	∘	∘	

expected $+1.88'$. This error was apparently caught on the floor; the available logs indicate that the test was actually performed at $+1.88'$. As noted in §D.7.2, the yaw axial reference was off by $-1'$ relative to the optical axis; thus, the actual off-axis angle for this test was yaw = $+0.88'$.

Table 14.3: Single Quadrant Pitch/Yaw values

Quadrant	energies	pitch($'$)	yaw($'$)
1T	Al, Ti	+3.56	+0.0
1N	Al, Ti	+0.0	+2.56†
1B	Al, Ti	−3.56	+0.0
1S	Al, Ti	+0.0	−4.56†
3T	Al, Fe	+2.87	+0.0
3N	Al, Fe	+0.0	+1.87†
3B	Al, Fe	−2.87	+0.0
3S	Al, Fe	+0.0	−3.87†
	Ti, Cr	+0.0	−2.87
4T	Al, Fe	+2.53	+0.0
4N	Al, Fe	+0.0	+1.53†
4B	Al, Fe	−2.53	+0.0
4S	Al, Fe, Cu	+0.0	−3.53†
	Ti, Cr	+0.0	−2.53
6T	Al, Fe, Cu	+1.88	+0.0
6N	Al, Fe	+0.0	+0.88
	Cu	+0.0	+0.88††
6B	Al, Fe	−1.88	+0.0
6S	Al, Fe, Cu	+0.0	−2.88†
	Ti, Cr	+0.0	−1.88

† Error of $1'$ in yaw zero reference

†† The CMDB indicates a yaw of $-1.88'$; other logs indicate that the HRMA was set to yaw = $+1.88'$. Adding the yaw axial offset error of $-1'$ gives yaw = $+0.88'$.

Pitching and yawing the HRMA allowed a better sampling of the length of the optic for a given shell shell and quadrant; at the same time, it complicates the interpretation of the data: in the on-axis case, the incident graze angle is nominally a function of the axial distance of the ray intercept along the optic. With the tilted optic, the graze angle varies with azimuth as well. Consequently,

the approach we take is to perform a raytraces which simulate the XRCF experiments as closely as possible. The raytraces were performed with the HRMA pitched or yawed according to the values as specified in the CMDB, but modified as necessary for the yaw reference error; see Table 14.3 and §D.7.2. The raytrace model was based on configuration `xrcf_SA01G+HD0S_HD0S-scat-980623_01`; note that this does *not* include finite source size effects or multilayer (and multilayer gradation) reflectivity effects. The smallest pinhole size used was 1 mm diameter, much larger than the projected source dimensions, so neglect of the finite source size is not significant in this case. The ("rough") multilayer reflectivity effects are of order 10%, small enough to be neglected in this first pass through the data analysis.

Currently, no mesh correction is applied to the raytrace simulations; again this is expected to be at most a 10% effect. As a test of this, a limited number of wing scan raytraces were performed including a simulation of the mesh (Table 14.4). As expected, the off-axis points are consistent with an overall mesh correction of about 10%. Note that the raytrace model currently underpredicts the measured wing scan X-ray data, so including the mesh correction will make the disagreement slightly worse.

Table 14.4: Effect of Mesh on Wing Scans

trwid	diam	iter	$N_{\rm nomesh}$	$N_{\rm mesh}$	ratio	error
D-IXF-PW-6.014a	1	0	914	884	0.967	0.046
D-IXF-PW-6.014a	1	1	2413	2327	0.965	0.028
D-IXF-PW-6.014a	1	2	7233	6970	0.964	0.016
D-IXF-PW-6.014a	1	3	922442	921402	0.999	0.0015
D-IXF-PW-6.014a	1	4	10019	8473	0.847	0.012
D-IXF-PW-6.014a	1	5	2984	2725	0.914	0.024
D-IXF-PW-6.014a	1	6	1059	969	0.915	0.041
D-IXF-PW-6.018	35	2	3098	2787	0.90	0.023
D-IXF-PW-6.018	35	3	1034352	1023056	0.989	0.0014
D-IXF-PW-6.018	35	4	2378	2124	0.89	0.027

14.1 Pinhole Effective Areas

The basic data obtained in the experiment were the effective areas measured for pinhole scans through the image. In this section we describe the reduction of the X-ray measurements and the raytrace simulation procedure.

14.1.1 X-ray data reduction

During Phase 1 at the XRCF, the HRMA effective area was measured at numerous spectral lines. The source used was the electron impact point source (EIPS). The anode selected, in concert with the high voltage used in the source, dictates the spectrum, both line and continuum, emitted by the source. Much of the continuum flux is absorbed by a filter placed between the source and the beam-line (and hence all the detectors). This filter is chosen in such a way as to have an optical depth of 2 or 4 at the line in question, and so it is optically much thicker at slightly higher energies where it has an absorption edge. Various pinholes can be positioned in front of the focal plane

detector to act as an aperture stop. In the wing scan experiments the pinhole diameters used were 1 mm, 4 mm, 10 mm, 20 mm, and 35 mm.

The pulse height spectral data were reduced using the method described in Chapter 9. Because the off-axis focal plane instrument often sees very low counting rates (only a few counts per bin) and can be dominated by background, we used the C-statistic ((Cash, 1979) and (Nousek and Shue, 1989)). We have also used the distributed gain double-`JMKmod` method (§9.4) to fit the BND-H data, which have relatively high signal-to-noise ratios.

The BND detectors are used to measure the photon flux density at the HRMA entrance, which is determined by dividing the count rate from each detector by the open area of its aperture (corrected for mesh transmission), and averaging the results. This average is then divided into the count rate from the focal plane detector, giving a quantity which has units of cm^2, known as the effective area. The quantities of interest here are the effective areas measured through pinholes positioned in front of the focal plane detector. In addition to the pinhole measurements in the wing scans, the on-axis effective area measured through a 35 mm pinhole was used to normalize the wing scan data; see the discussion below.

14.1.2 Raytrace simulations of the pinhole experiments

The wing scan raytraces were performed as very long raytraces (incident ray density of 500 rays/mm^2) in which the rays were processed by the `pinhole` module. The `pinhole` module tallies the total number of rays and total ray weight for rays which would have passed through a virtual pinhole with a given radius and position. An array of (possibly overlapping) virtual pinholes of arbitrary sizes can be processed together. In these simulations, the rays were processed through pinholes positioned between −105 mm and +105 mm with 0.1 mm spacing, for pinhole diameters 1, 4, 10, 20, and 35 mm. In each case the conditions of the actual X-ray experiment were replicated as well as possible including the finite X-ray source distance and the pitch or yaw of the HRMA. The quadrant shutters were modeled using opaque apertures shaped and positioned according to the specifications of the aperture assembly drawings (aperture `quad_shutter_05.lua`).

The pinhole effective areas were evaluated by dividing the total ray weight for rays passing through the pinhole by the known ray density at the HRMA entrance. The statistical error on the pinhole effective area was estimated by dividing the pinhole effective area by the square root of the number of rays passing through the pinhole (appropriate for Poisson statistics).

14.2 The Experiment as Performed

The analysis of the wing scan experiment was complicated by several aspects of the as-run experiment. In particular, the execution of the pinhole experiments with nonzero HRMA pitch resulted in a shift of the HRMA focus which was not (for the most part) captured by the FOA tables; consequently, the distance between pinhole center and focus based only on the HXDA stage logs and the FOA table in many cases needs to have a pitch correction applied. In addition, the confusion engendered by the built-in HRMA decenter error (Coma-free decenter; see Chapter 30) resulted in the HRMA bore sight being offset by $1'$ in yaw for part of the testing; as a result, in some cases the actual yaw values differed by $1'$ from the intended values (*i.e.*, those requested in the CMDB). Finally, the mapping of the wings relies on using the quadrant shutters to isolate individual mirror shells and quadrants. Some of the pinhole scans reach sufficiently far off-axis that vignetting by closed shutters for adjacent shells becomes important, particularly for shells 3 and 4 which are physically close together. These issues are addressed in more detail in the following sections.

14.2.1 History of the Pitch Problem

For the XRCF data, the pinhole positions relative to the focus were calculated using `calcstage4`. In the `calcstage4` calculation the pinhole location relative to the focus is determined by using the stage logs and the contemporaneous focus position appropriate to the shell(s) in use is determined from the FOA tables. The distance (X, Y, Z) of the pinhole from the focus is evaluated by differencing the two sets of values:

$$X = X_{pinhole} - X_{focus} \tag{14.1}$$
$$Y = Y_{pinhole} - Y_{focus} \tag{14.2}$$
$$Z = Z_{pinhole} - Z_{focus} \tag{14.3}$$

Note that currently the only information that `calcstage4` has about the focus position is that found in the FOA tables; if the FOA table is incorrect about where the focus happens to be, then `calcstage4` will get the wrong answer.

Because an aft vertical actuator was stuck during phase 1E, pitch motions during phase 1E were carried out using only the forward vertical actuator. This resulted in a pitch motion about a point other than the HRMA node, so any pitch motions caused the HRMA node (and hence, the finite conjugate focal point) to shift vertically. These vertical shifts in focus location can be large ($\lesssim 1$ mm) compared to the size of the smallest pinhole used in the wing scans (1 mm diameter). It is therefore important to understand the relation between HRMA pitch moves and the FOA tables.

In order to determine how the experiment was really performed, the XRCF 2nd Floor Shift Reports, the Project Science/Telescope Scientist logs, and the EKC shift reports were examined. The first wing scan experiment in Phase 1E was a wing scan of quadrant 6B with an EIPS C-Kα source and with the HRMA pitched by $-1.88'$. A set of Y-scans was performed (E-IXF-PW-2.001–5, day 028/029) followed by a set of Z-scans (E-IXF-PW-2.010–13, day 029). During the the first sequence of 1 mm pinhole Y-scan measurements (E-IXF-PW-2.001) it was discovered that the scan was approximately 500 μm too low. It was realized that this was because the pinhole positions were calculated relative to the FOA values for the focus position and that the FOA value was now offset from the real focus of the pitched HRMA. In order to compensate for this, the FOA table was adjusted by 504 μm in Z for the rest of the quadrant 6B C-Kα wing scans (4 mm, 10 mm, 20 mm, 35 mm Y-scans, 1 mm, 4 mm, 10 mm, 20 mm Z-scans) based on a beam centering with the 70 μm pinhole. Following the C-Kα wing scans, the FOA values were reset back to the nominal values. The actual pitch correction should have been 609 μm in Z, so the FOA table correction was about 105 μm shy of the appropriate correction. Consequently, the `calcstage4` values for the distance of the pinhole from the focus were nearly correct for these pinholes, but additional $\Delta Z_{focus} = +105$ μm pitch correction needs to be applied. (The additional pitch correction we actually applied was $\Delta Z_{focus} = +94$ μm; the effect of the remaining 11 μm discrepency is negligible for these wing scan measurements.)

It was initially suggested that a similar FOA adjustment be made for all the subsequent HRMA pitch moves. It was decided instead to aim for an automated approach whereby the pitch correction would be applied to the pinhole locations during the CMDB processing; these fixes were incorporated into the software during shift A, 1997 Feb 2 (day 033). Note that for the period between the end of the 6B C-Kα wing scans on day 029 and CMDB fixes of day 033, any pitch corrections would have been entered manually into the pinhole locations files.

Node Shift in HRMA Pitch Moves

Because the HRMA pitch motions were performed with the aft vertical actuators fixed, the actual pitch motion was a rotation about the line defined by the aft vertical actuator locations. This produced a vertical shift of the HRMA node which displaced the focal point at the instrument plane.

In comparing the raytraces to the XRCF pinhole data, the XRCF Z coordinates relative to the contemporary FOA were corrected for the shift in the focus by subtracting off a pitch correction. To first order, the vertical shift in the node is the product of the sine of the pitch angle change and the axial offset between the fixed actuator station and the node. The axial distance between the node and the actuator is 43 inches (= 1092.2 mm), from which

$$\Delta Z_{node} = -1092.2 \ \sin\Delta\theta_{pitch} \text{ mm} \tag{14.4}$$

where $\Delta\theta_{pitch}$ is the change (in radians) in the HRMA pitch. In the thin lens approximation, the focus moves by

$$\Delta Z_{focus} = \frac{\Delta Z_{node}}{D_{source}} \times (D_{source} + D_{focus}) \tag{14.5}$$

where $D_{source} = 527297$ mm is the distance between the HRMA node and the X-ray source, and $D_{focus} = 10256$ mm is the nominal distance from the HRMA node to the finite conjugate focus. In making the above estimates, the node was assumed to be 18.1 mm aft of CAP "Datum A". Substituting for the various distances, the vertical shift in focus is approximately:

$$\Delta Z_{focus} = -1.1134 \times 10^6 \sin\theta_{pitch} \ \mu\text{m} \tag{14.6}$$

or,

$$\frac{\Delta Z_{focus}}{\Delta\theta_{pitch}} \simeq -323.9 \ \mu\text{m/arcmin}. \tag{14.7}$$

Pitch Corrections Applied

Most of the wing scans with HRMA at nonzero pitch were performed with the FOA table values appropriate to HRMA at zero pitch; the requisite pitch corrections were applied to the requested pinhole locations. `calcstage4` calculates the pinhole location based on the stage logs; the resulting physical location for the pinhole will be calculated correctly. In analyzing the wing scans, the distance of the pinhole center from the current focal point is needed; the `calcstage4` evaluation of the focus position is based on the FOA entry and that is incorrect because of the HRMA node shift (and resultant shift in focus). `calcstage4` reports the difference between the pinhole location and the focus position, so a pitch correction needs to be *subtracted* from the `calcstage4` Z value. Based on equation (Eq. D.6), the pinhole Z value reported by `calcstage4` was corrected by

$$\Delta Z_{corr} = Z - \Delta Z_{focus}. \tag{14.8}$$

An exception was the wing scan for shell 6B for which the FOA was partially compensated for the pitch-induced focus change (§D.7.1); in this case, the Z values were corrected by -94 μm to account for the slight undercorrection of the FOA adjustment.

14.2.2 Yaw Reference Error

Early in Phase 1D, an attempt was made to determine the HRMA X-ray bore sight by using the variation of effective area as the HRMA was pitched and yawed. At the time, the presence of the coma-free decenter error in the HRMA mirror alignment was not yet known; this error causes the off-axis effective area profiles to be nonsymmetric about the optical axis. This led to an initial confusion as to alignment of the mirror bore sight to the facility optical axis; the reference axis for pitch and yaw ended up being offset by about $1'$ in yaw starting at IAP 5 (day 005, 16:11) through the end of phase 1D. Consequently, the actual yaws ended up being offset by $1'$ from the requested values, and because of this, some yaw values in Table 14.3 differ from the requested CMDB values. This does not directly affect the XRCF data reduction; the yaws were off, but the FOA was determined based on the contemporary yaw zero reference. However, this offset does need to be included in the comparison raytraces.

14.2.3 Vignetting by Quadrant Shutters

In the plots of pinhole effective areas, the raytrace results are displayed at 0.1 mm intervals for the 1 mm diameter pinhole, 0.4 mm intervals for the 4 mm pinhole, and at 1 mm intervals for the 10, 20, and 35 mm pinholes.

Although the scattering formulation currently being used in the raytracing is symmetric with regard to scattering toward or away from the surface, the raytrace pinhole effective areas do show an asymmetry in deflections towards or away from the mirror surface. This is at least in part because of the off-axis vignetting by the quadrant shutter blades. The quadrant shutter vignetting is particularly noticeable in the larger pinholes for shells 3 and 4; see Figure 14.1. In Figure 14.2 the results *for a single mirror pair*, MP3, are compared with only the 3S quadrant open and with the all the S quadrants open. (This latter experiment could not be done at XRCF because closing the 1S, 4S, and 6S shutters is necessary in order to isolate shell 3.) It is evident that the 1S and 4S shutter blades can significantly vignette the wing scan observations for shell 3S; similar observations apply to the other shells.

The reason for the drop-off away from the mirror (shell 3) or towards the mirror (shell 4) can be seen in Figure 14.3. In this figure, ray position *vs.* ray azimuth is plotted at the axial location for the quadrant shutters. In each case, only one quadrant shutter is open. The horizontal and vertical lines indicate the limiting edges of the adjacent shutter blades. For 35 mm diameter pinholes, shell 3 begins to be vignetted by the adjacent shell 4 shutter blade by the time the pinhole is only 30 mm off-axis. Note that at the shutter assembly position, the X-rays are on cones converging towards the focus. Consequently, scattering towards the mirror surface shows up as deflections towards larger radius at the shutter plane; similarly scattering away from the mirror surface produces deflections towards smaller radius at the shutter plane.

14.3 Pinhole Effective Areas: X-ray data *vs* Raytrace

The effective area through a pinhole of a given radius as a function of the pinhole off-axis position provides the most direct comparison between the XRCF data and the raytrace simulations. The X-ray data and the raytrace pinhole effective areas are compared in the following subsections. Each page provides plots comparing the XRCF data *vs.* raytrace data for different pinhole diameters for a given shell, quadrant, and energy; the figures are presented in the order: shell, quadrant (T, N, B, or S), and energy.

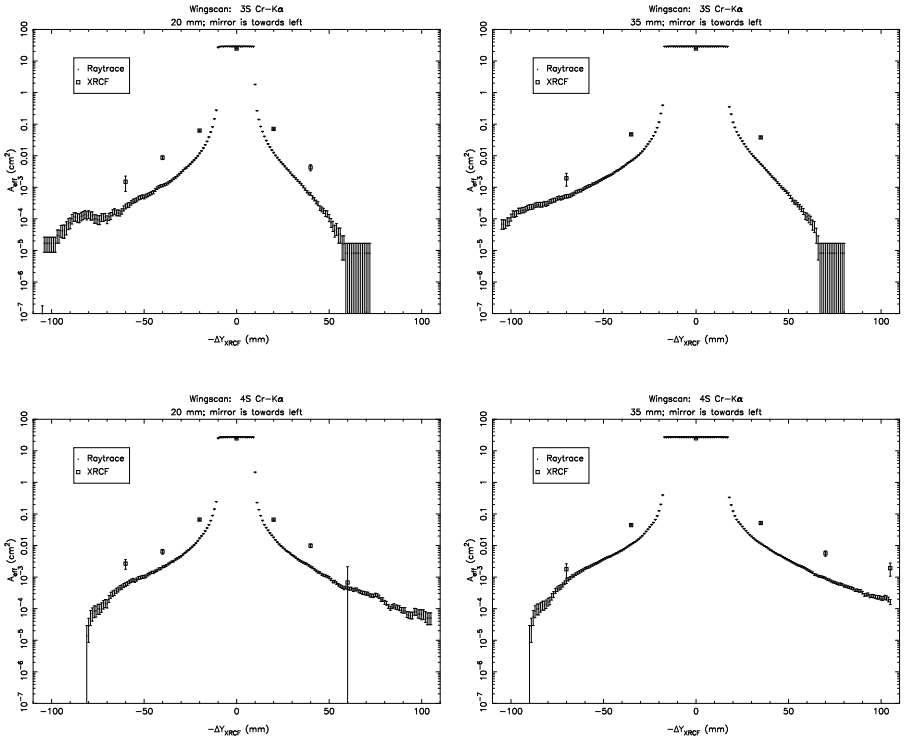

Figure 14.1: Effect of quadrant shutter vignetting: shell 3 *vs.* shell 4. Note that Shell 3 is vignetted away from the mirror while shell 4 is vignetted towards the mirror, consistent with Figure 14.3.

14.3.1 Single Quadrant Wing Scan Pinhole Data

In this section the XRCF single quadrant wing scan pinhole effective area measurements are compared to the raytrace simulations of the same configurations. The list of sampled pinhole measurements is summarized in Table 14.1. In the plots of pinhole effective areas, all the XRCF data points are plotted. The raytrace results are displayed at 0.1 mm intervals for the 1 mm diameter pinhole, 0.4 mm intervals for the 4 mm pinhole, and at 1 mm intervals for the 10, 20, and 35 mm pinholes (see Chapter 14).

The central portion of the profile appears flat up to a distance of about half the pinhole diameter away from the center; in this regime, the sharply peaked core of the PSF falls entire within the pinhole and the effective area varies slowly as different portions of the wings are included together with the core. The pinhole effective area drops off rapidly as the core moves outside the pinhole, then more slowly as the near-wings of the PSF are also excluded from the pinhole. The wing scan experiment is concerned with the outer wings of the PSF.

For the smallest pinholes, the agreement with the raytrace simulations is often quite good. The distribution is often approximately symmetric about the center (for example, 1T Ti-Kα, Figure 14.8), (for example, 1S Al-Kα, Figure 14.7), but markedly asymmetric in other cases, (for example, 4S Al-Kα, Figure 14.25). In the cases with marked asymmetry, the point(s) in the direction corresponding to scattering away from the mirror surface tend to be higher than those towards the mirror surface. A notable exception is the 6B C-Kα in-plane scan. The distribution for the 1 mm pinhole looks reasonably symmetric, but in the 4 mm scan, the point 4 mm inwards is an order of magnitude higher than the point 4 mm outwards. (The central point was omitted for the 4, 10, and 20 mm scans; no 35 mm scan was done in this case.) Examination of the raw data indicates that the difference is real; the available information on pinhole positions and tolerances indicate that these are accurate as well. Currently we have no explanation for this difference. (See also the 6B C-Kα out-of-plane scan (§14.3.2) which took place immediately prior to the in-plane scan.)

In general, the agreement between the X-ray data and the simulations gets worse for larger off-axis angles, particularly for the larger pinholes. The raytrace simulations for the larger pinholes also show effects of vignetting by the adjacent quadrant shutter blades (see Chapter 14 for further details.)

Further analysis of the wing scan experiment (including derivation of surface brightness profiles

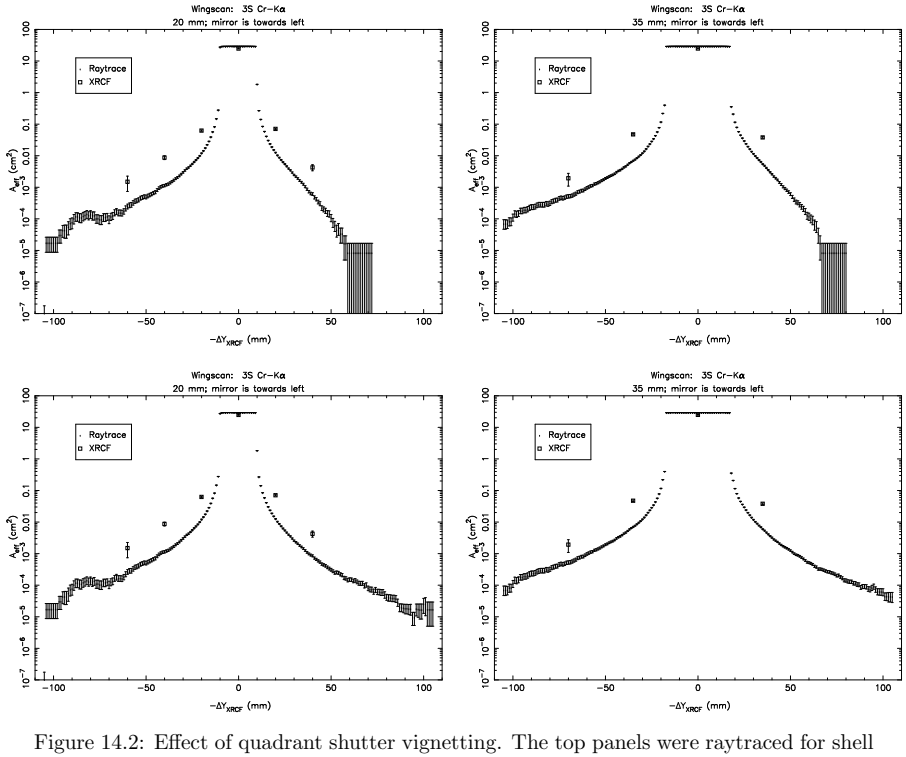

Figure 14.2: Effect of quadrant shutter vignetting. The top panels were raytraced for shell 3 alone and with quadrant configuration `cccc-ccco-cccc-cccc` while the bottom panels were traced with shell 3 alone but with all the South shutters open (quadrant shutter configuration `ccco-ccco-ccco-ccco`).

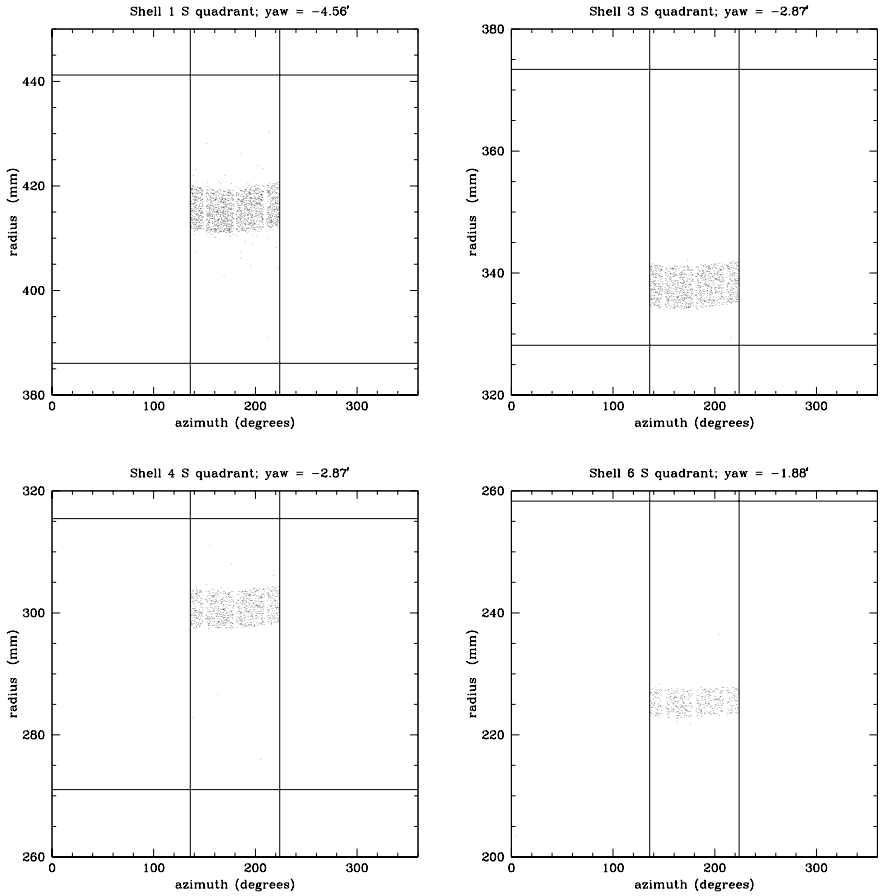

Figure 14.3: Quadrant shutter vignetting. The figures are spot diagrams for ray positions at the planes of the quadrant shutter blades. The vertical and horizontal lines indicate the limiting edges for the adjacent, closed quadrant shutters. Top Left: 1S (configuration `ccco-cccc-cccc-cccc`). Top Right: 3S (configuration `cccc-ccco-cccc-cccc`). Bottom Left: 4S (configuration `cccc-cccc-ccco-cccc`). Bottom Right: 6S (configuration `cccc-cccc-cccc-ccco`).

and corresponding PSD's) is provided in Chapter 15.

Shell 1 Single Quadrant Scans

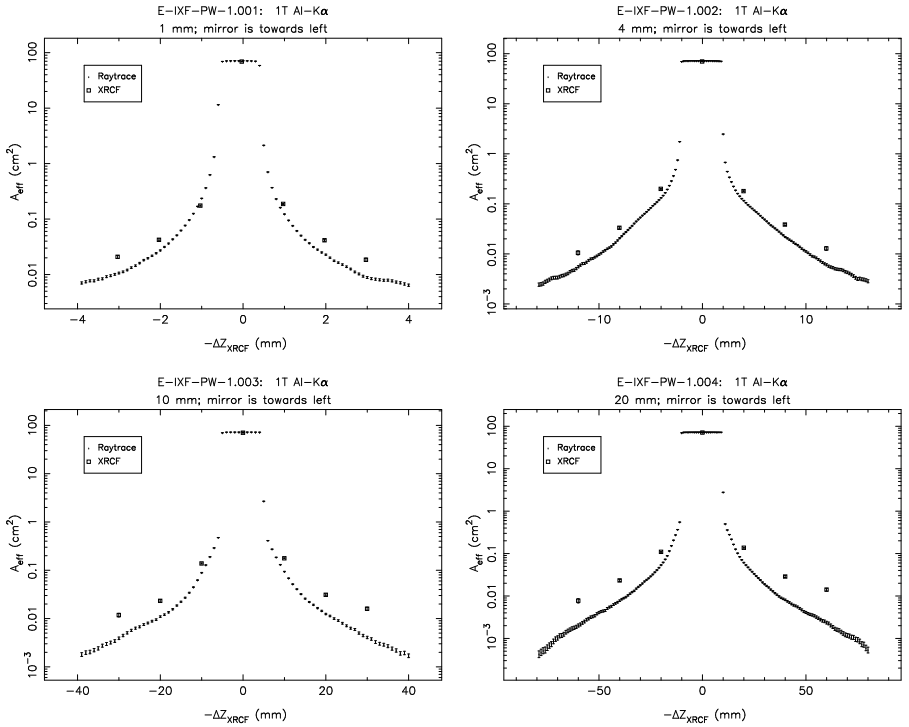

Figure 14.4: Pinhole effective areas; Shell 1T at Al-Kα.

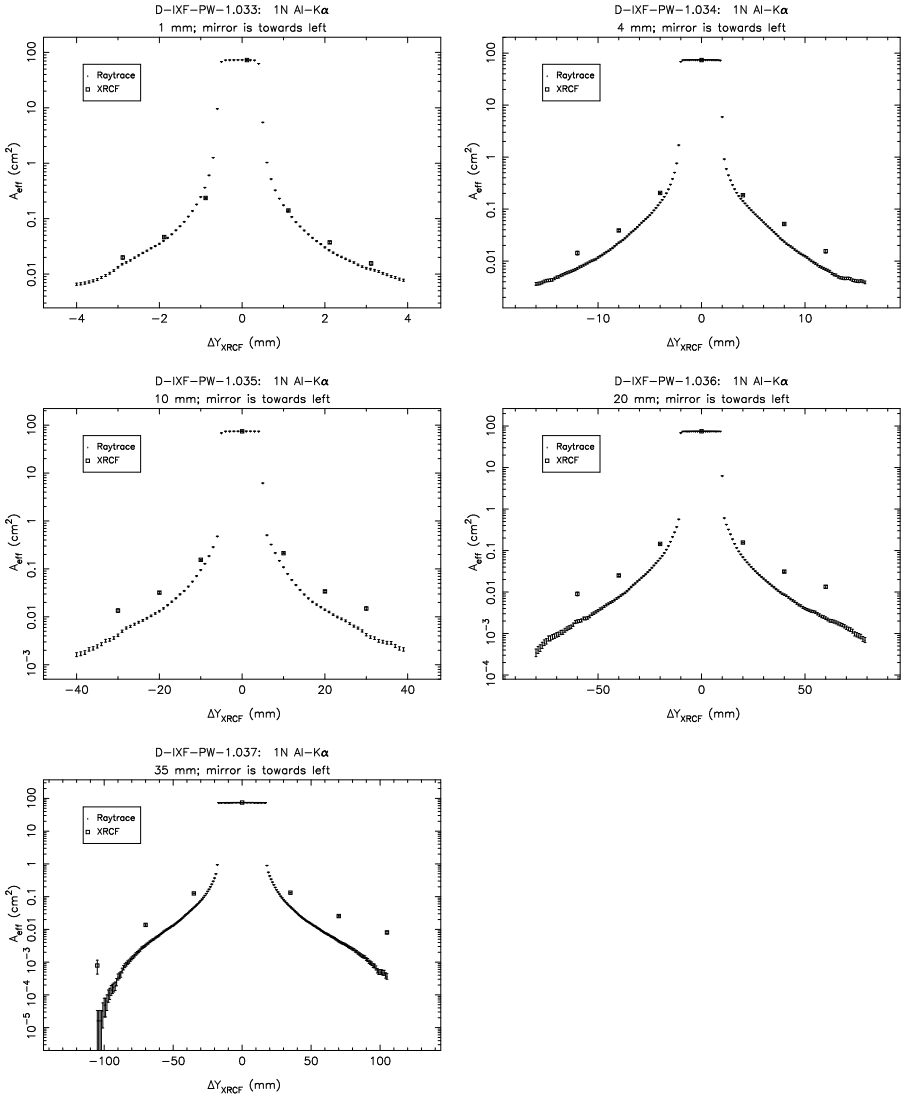

Figure 14.5: Pinhole effective areas; Shell 1N at Al-Kα.

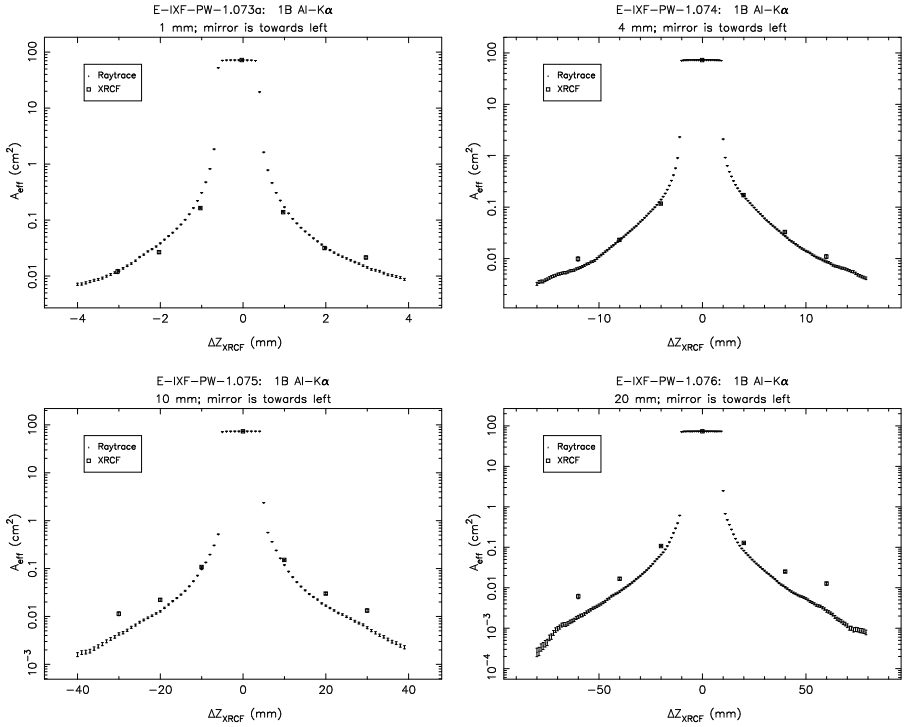

Figure 14.6: Pinhole effective areas; Shell 1B at Al-Kα.

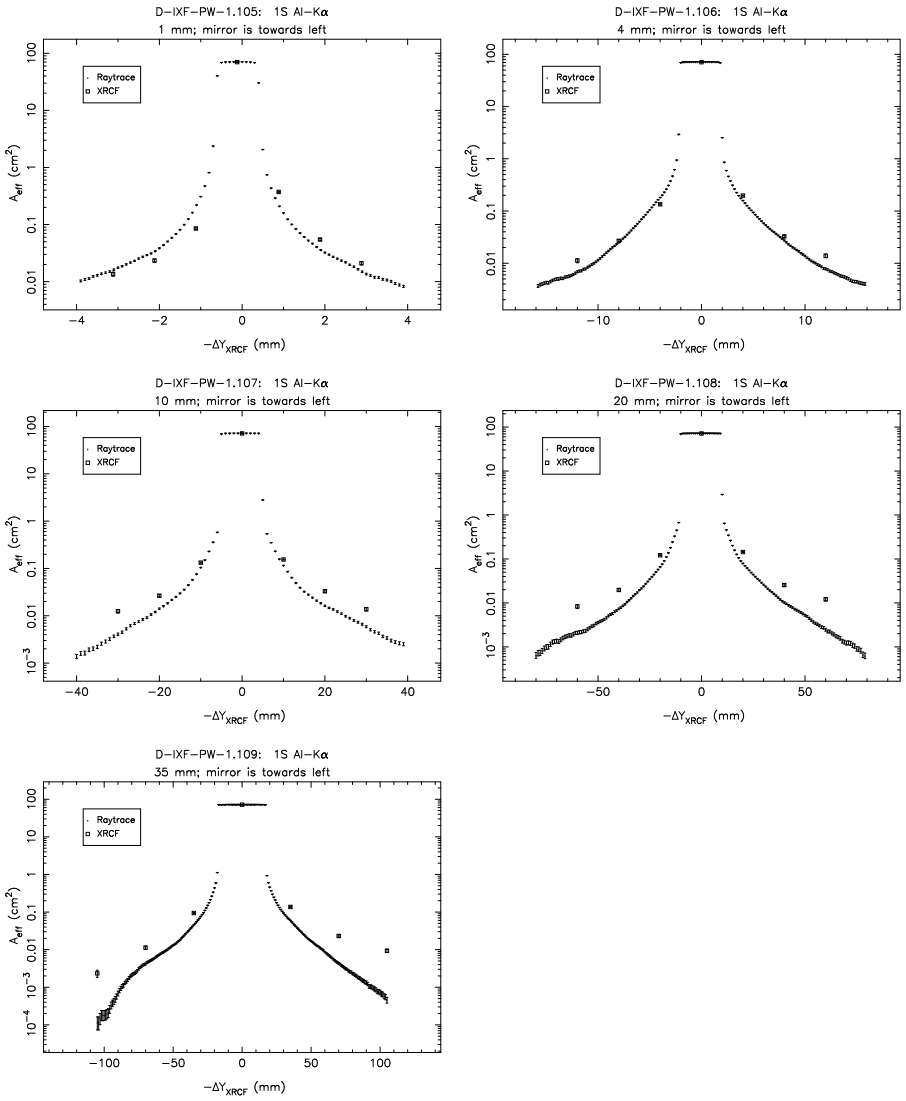

Figure 14.7: Pinhole effective areas; Shell 1S at Al-Kα.

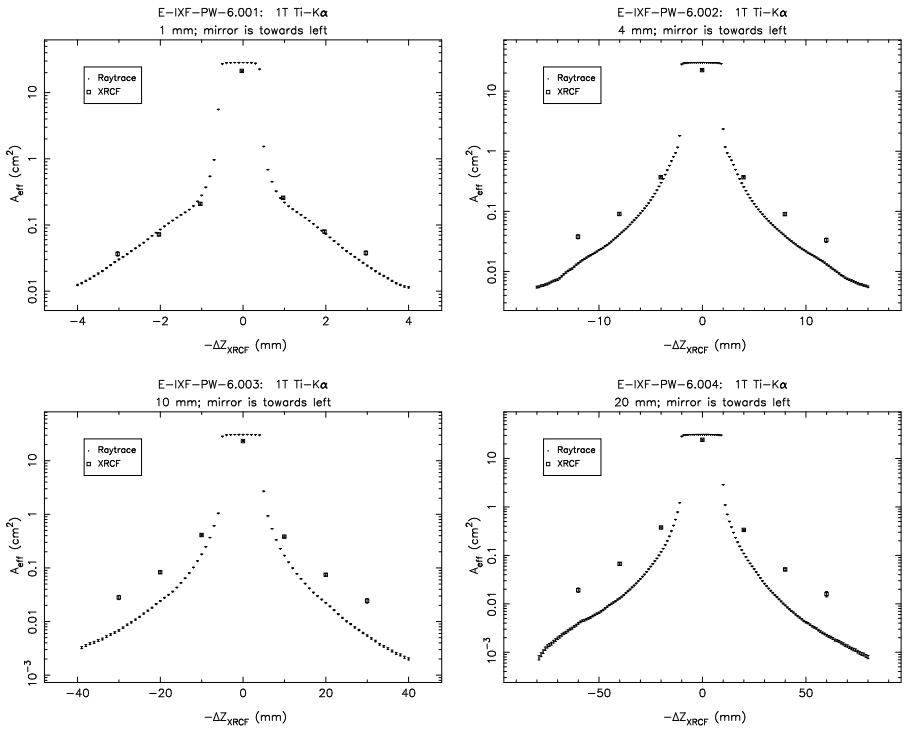

Figure 14.8: Pinhole effective areas; Shell 1T at Ti-Kα.

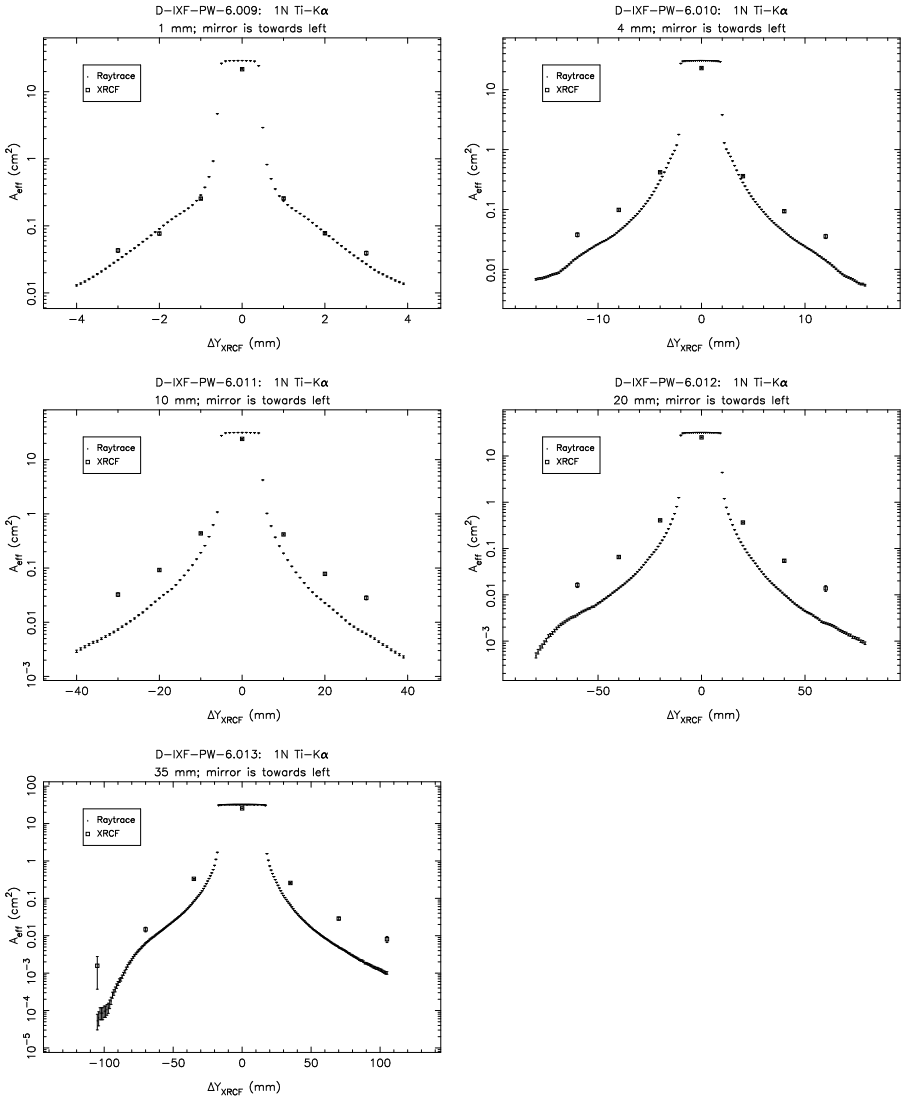

Figure 14.9: Pinhole effective areas; Shell 1N at Ti-Kα.

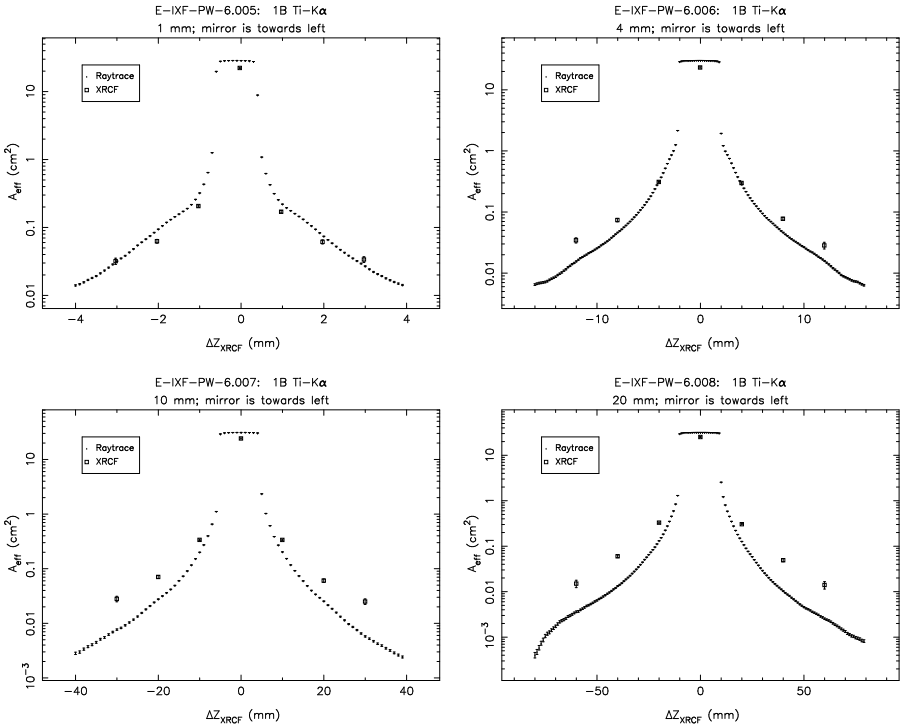

Figure 14.10: Pinhole effective areas; Shell 1B at Ti-Kα.

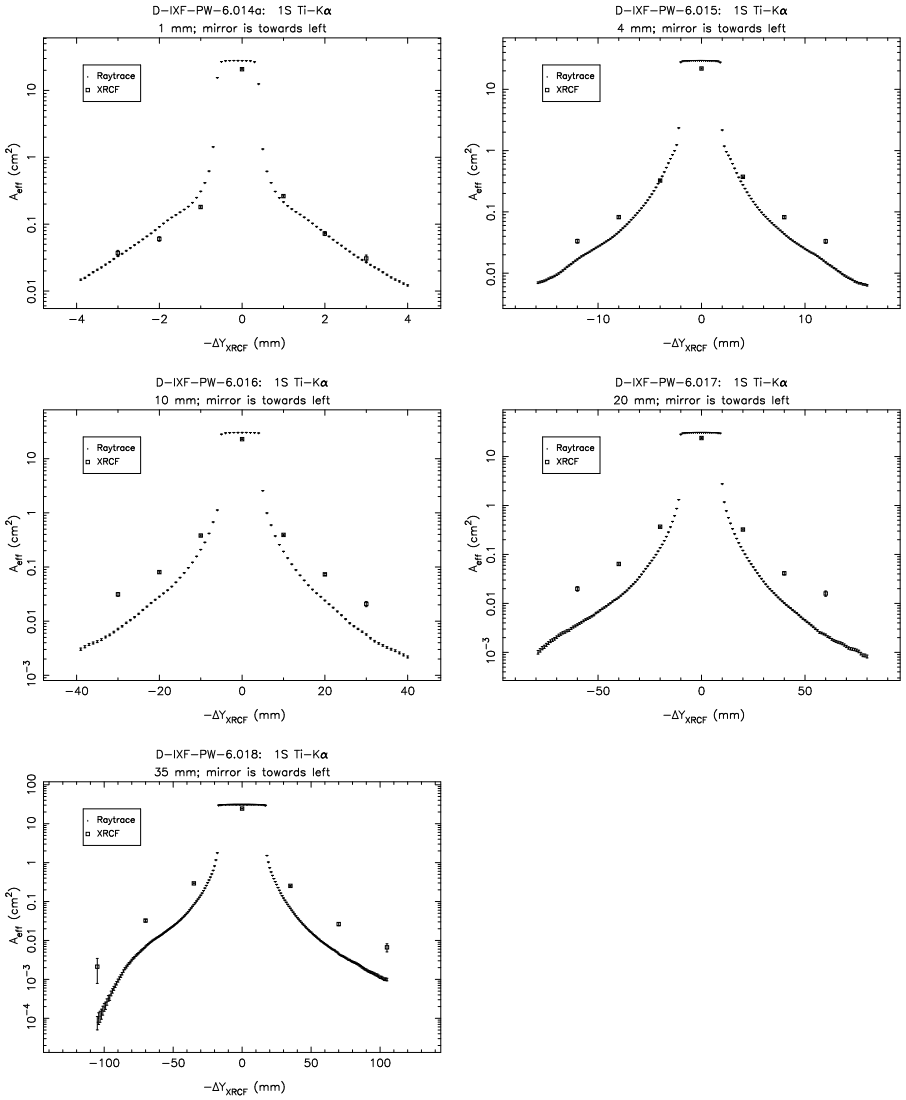

Figure 14.11: Pinhole effective areas; Shell 1S at Ti-Kα.

Shell 3 Single Quadrant Scans

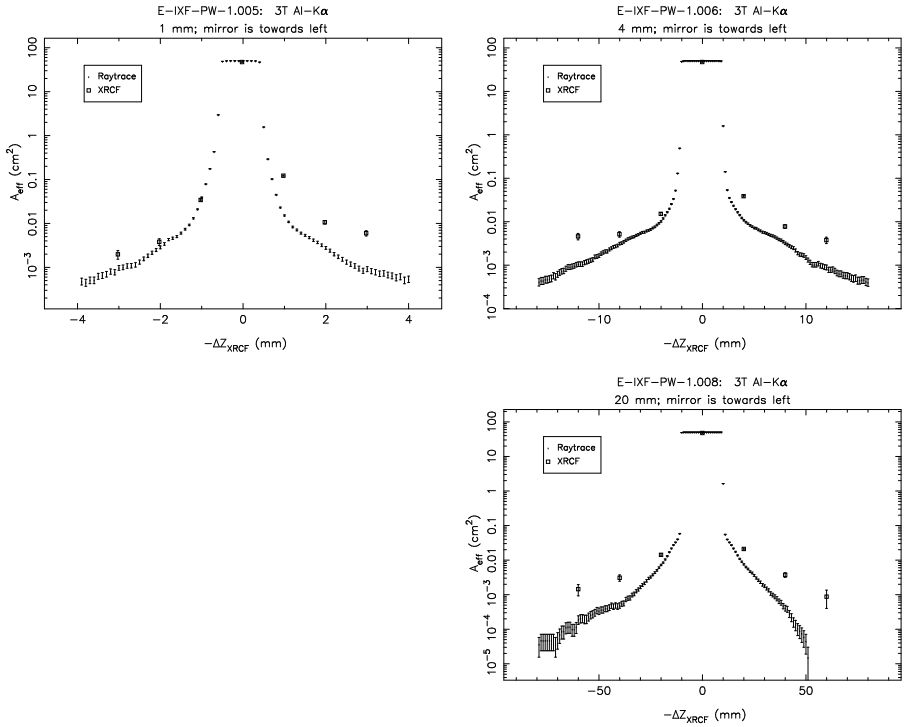

Figure 14.12: Pinhole effective areas; Shell 3T at Al-Kα.

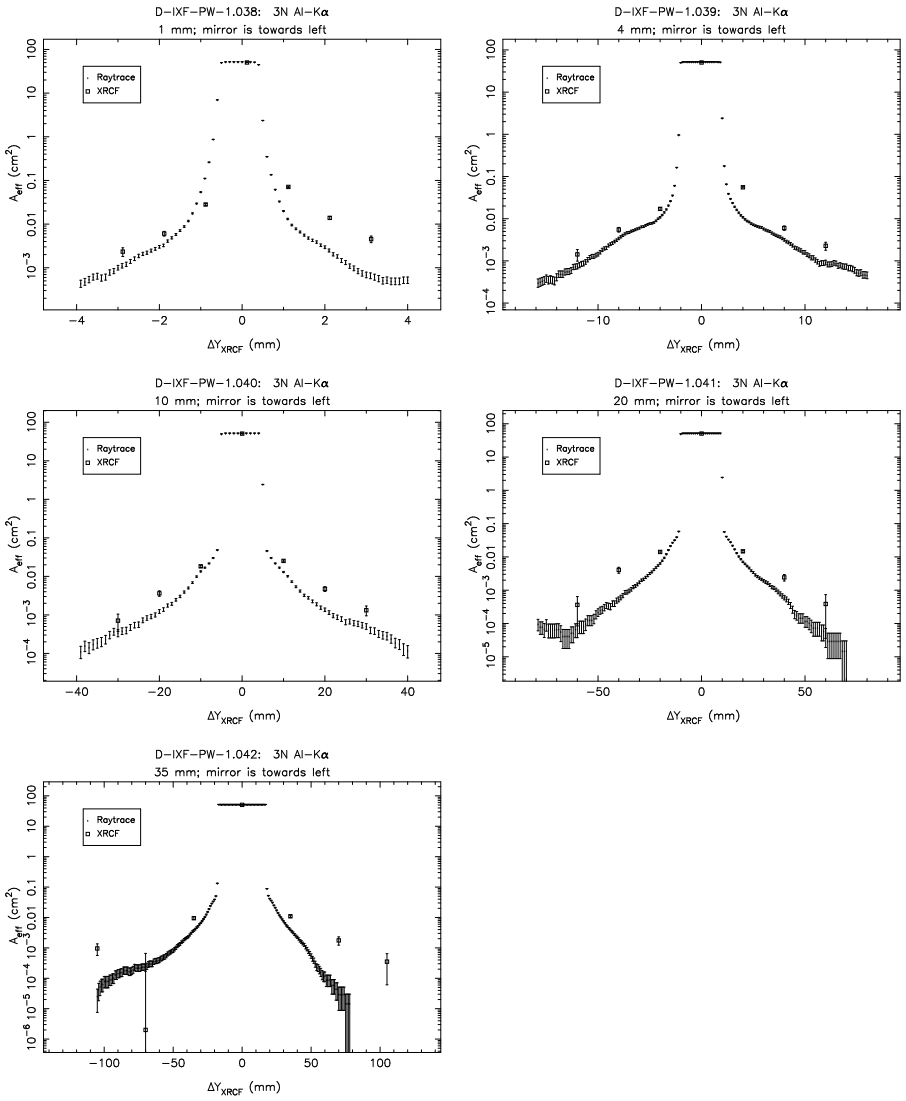

Figure 14.13: Pinhole effective areas; Shell 3N at Al-Kα.

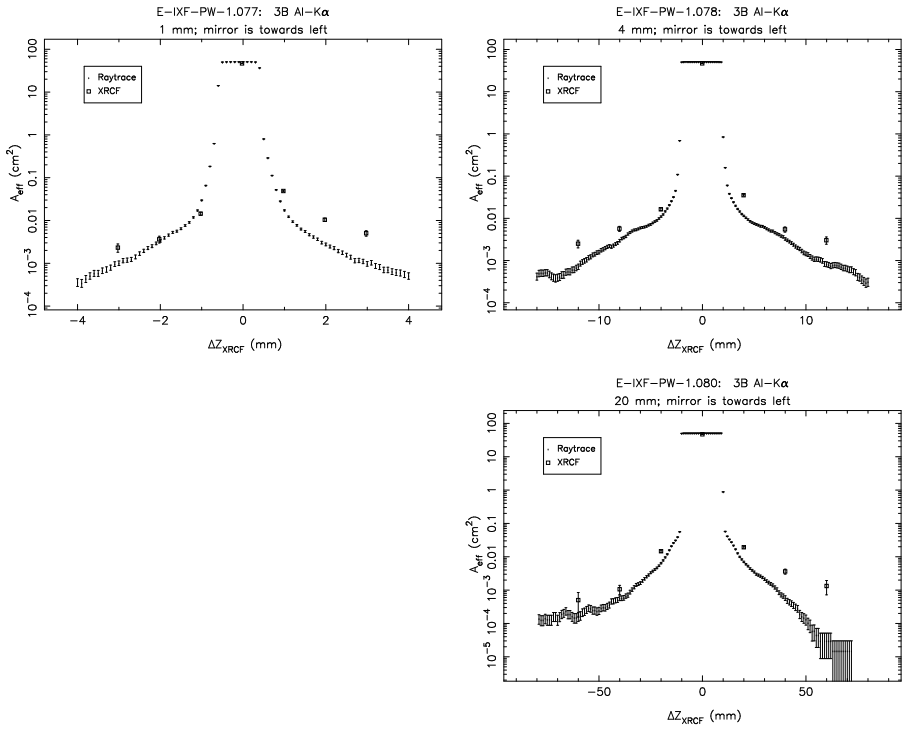

Figure 14.14: Pinhole effective areas; Shell 3B at Al-Kα.

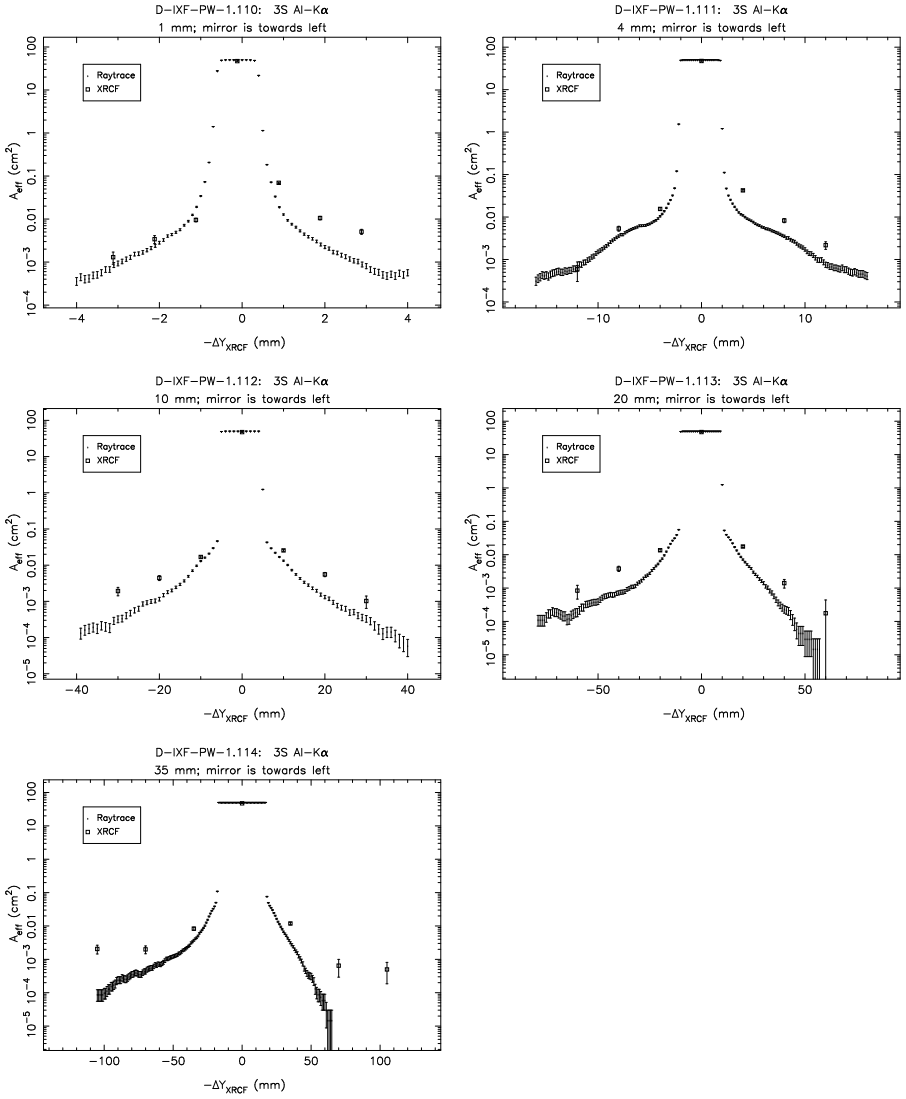

Figure 14.15: Pinhole effective areas; Shell 3S at Al-Kα.

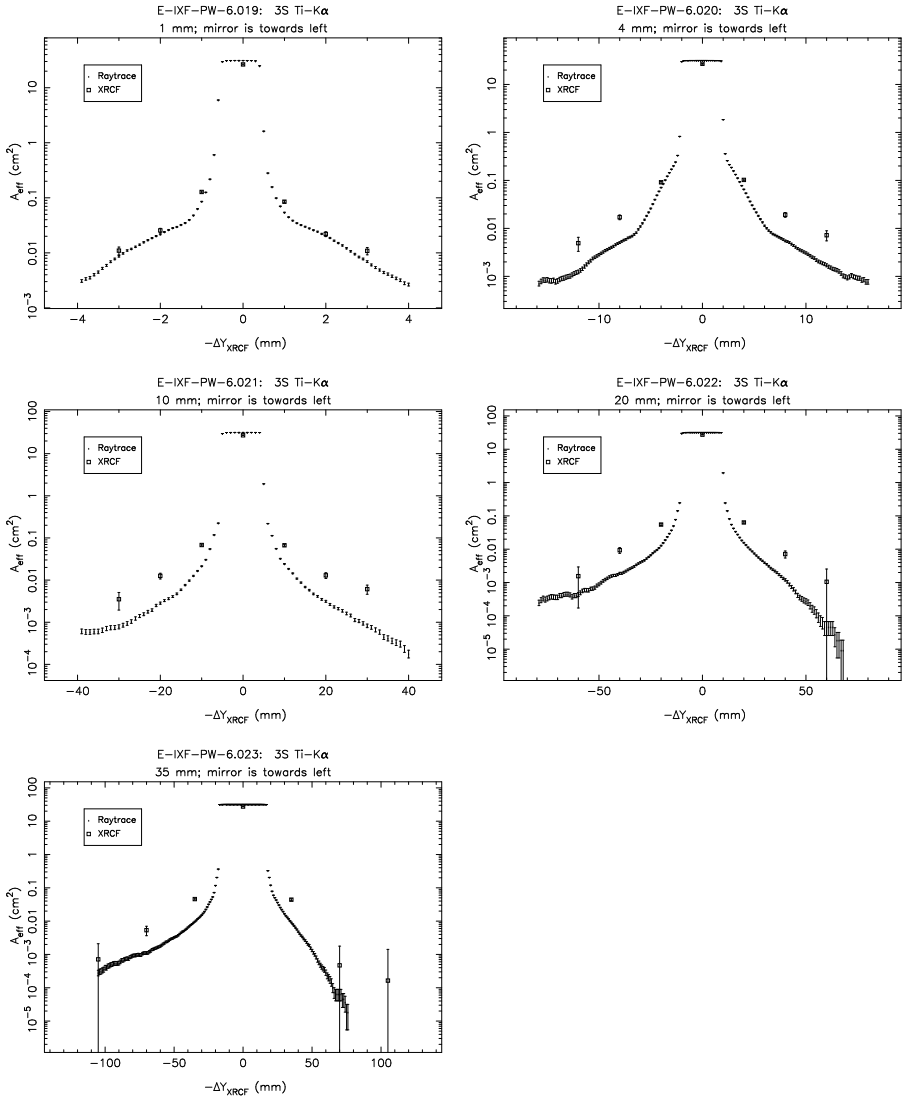

Figure 14.16: Pinhole effective areas; Shell 3S at Ti-Kα.

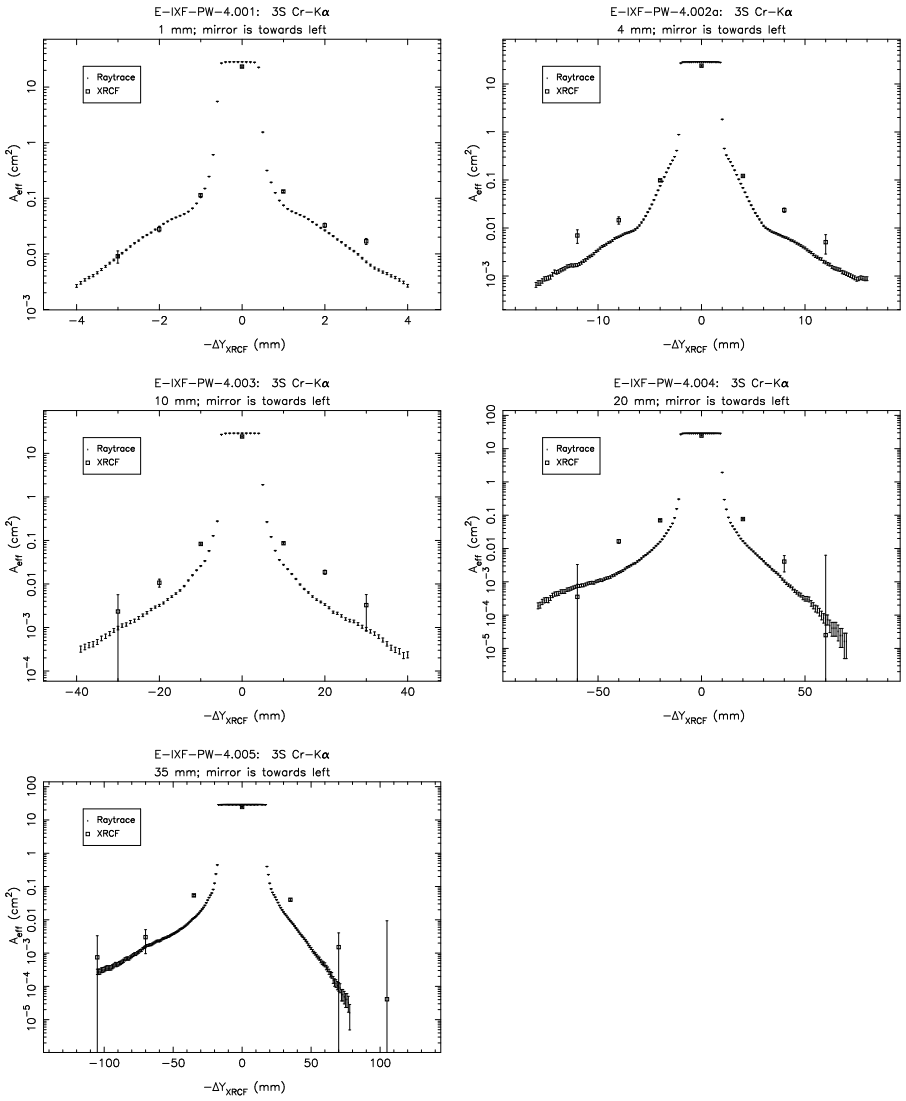

Figure 14.17: Pinhole effective areas; Shell 3S at Cr-Kα.

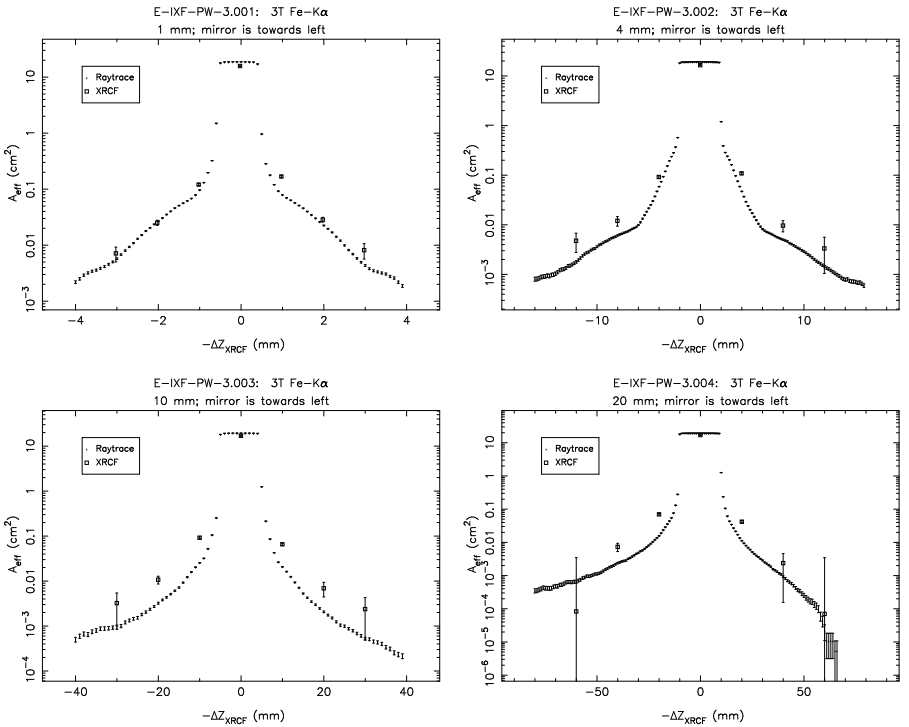

Figure 14.18: Pinhole effective areas; Shell 3T at Fe-Kα.

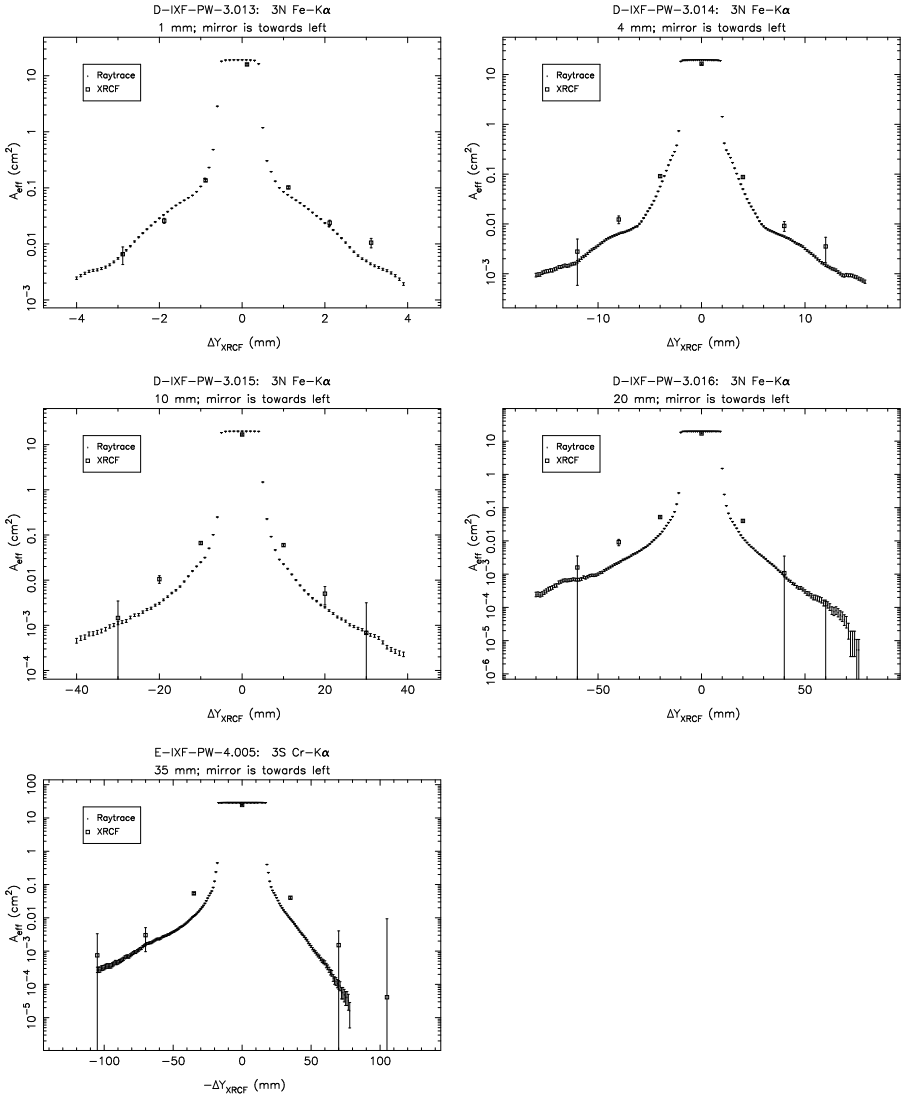

Figure 14.19: Pinhole effective areas; Shell 3N at Fe-Kα.

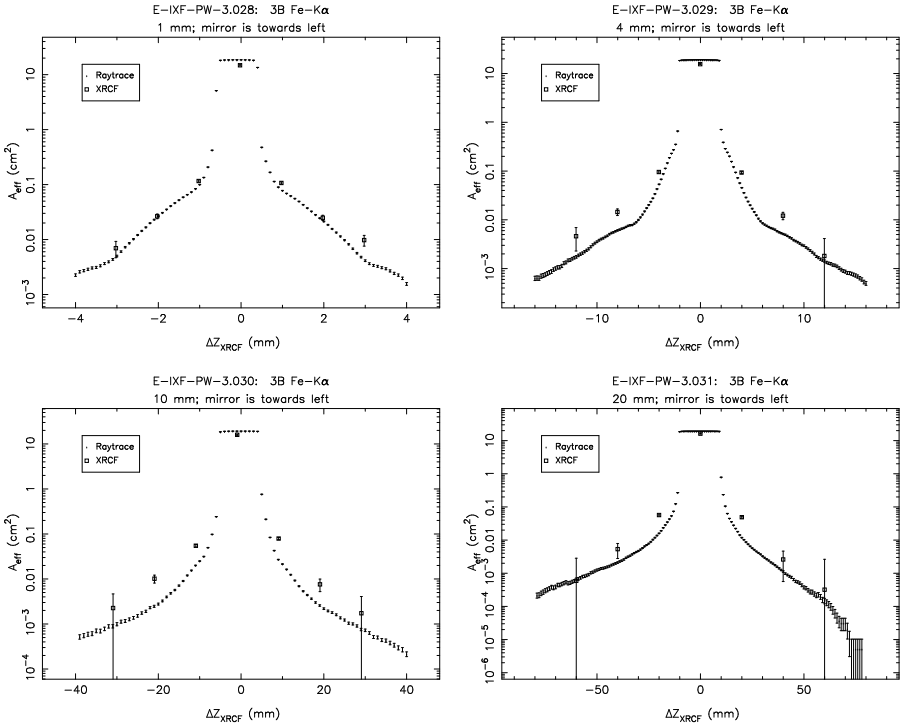

Figure 14.20: Pinhole effective areas; Shell 3B at Fe-Kα.

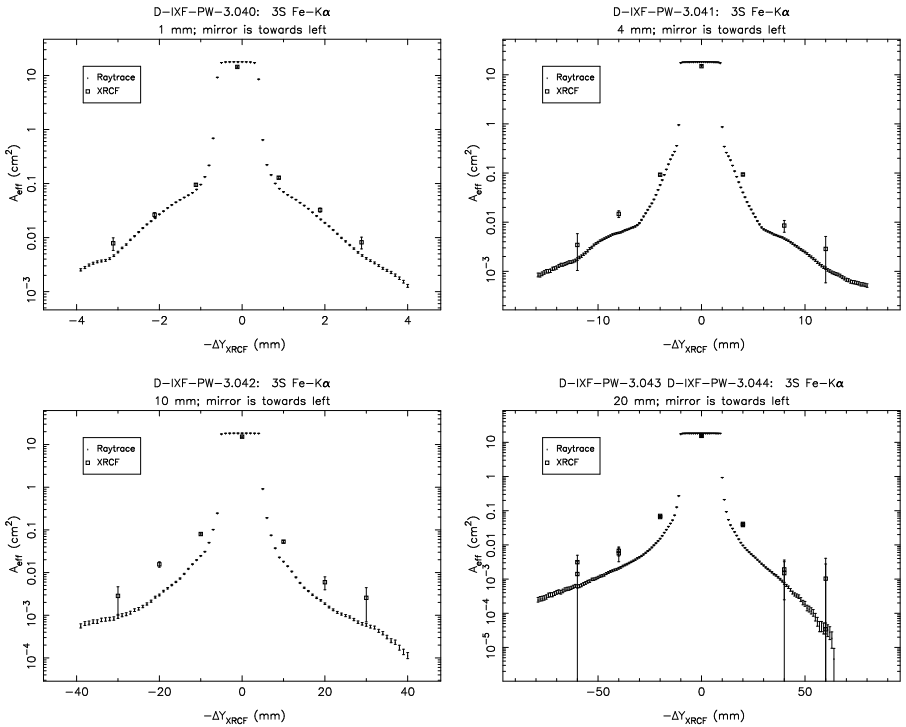

Figure 14.21: Pinhole effective areas; Shell 3S at Fe-Kα.

Shell 4 Single Quadrant Scans

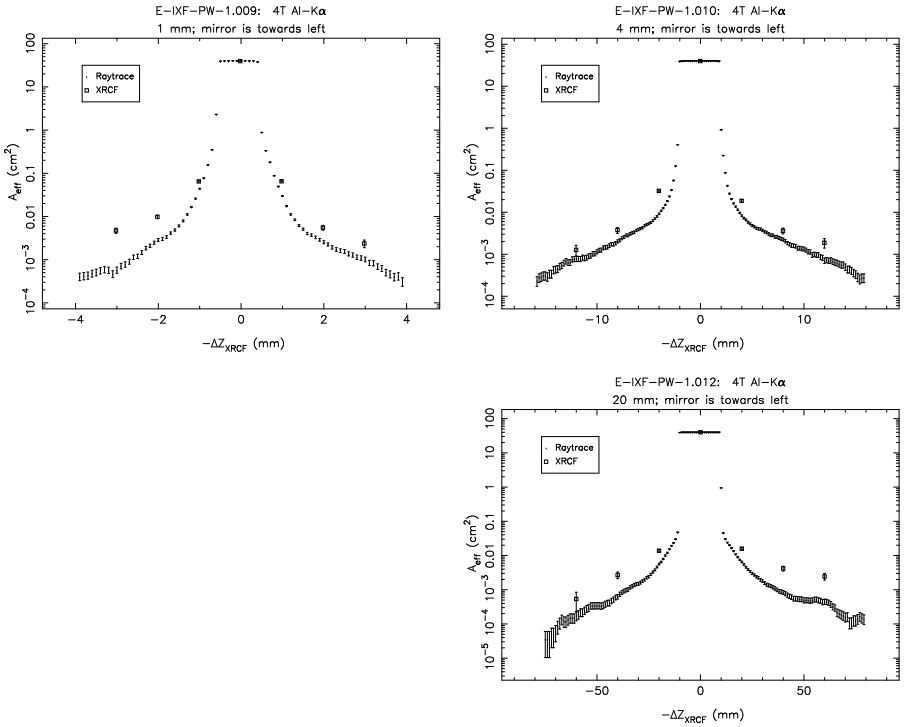

Figure 14.22: Pinhole effective areas; Shell 4T at Al-Kα.

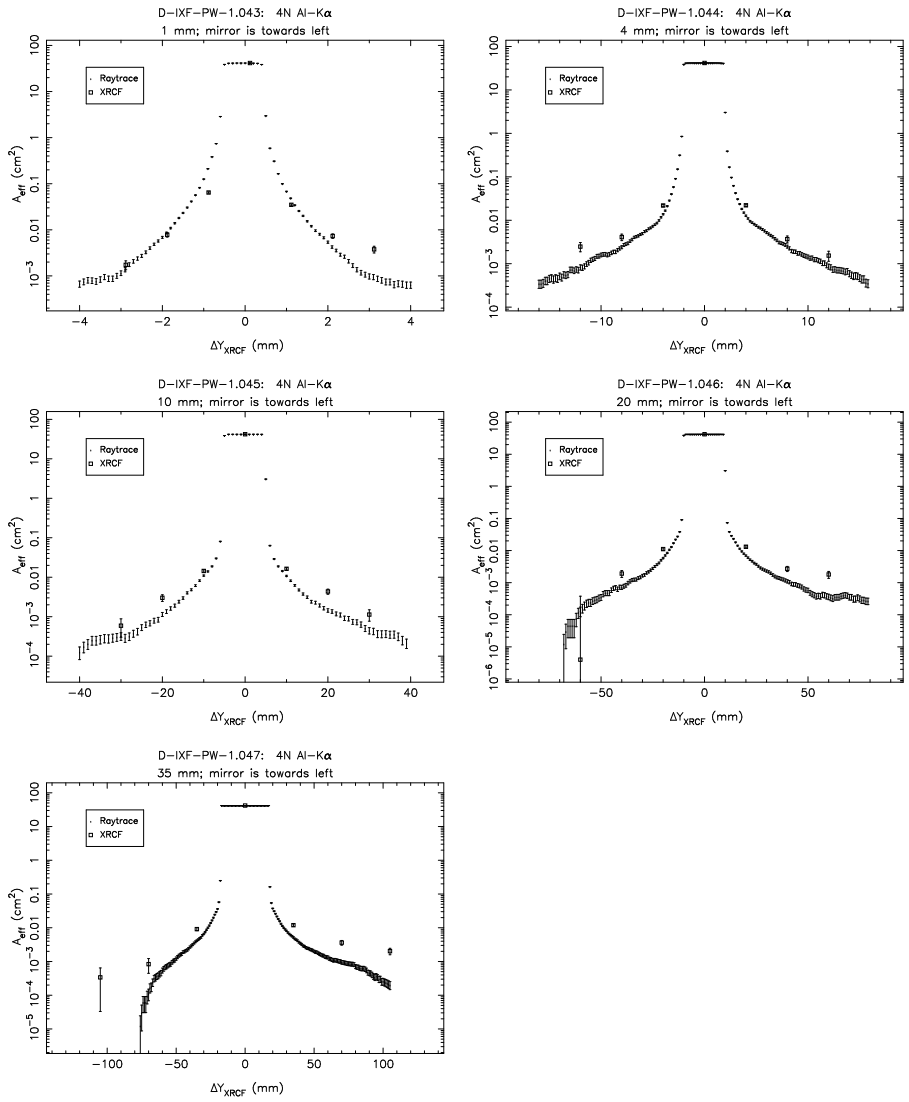

Figure 14.23: Pinhole effective areas; Shell 4N at Al-Kα.

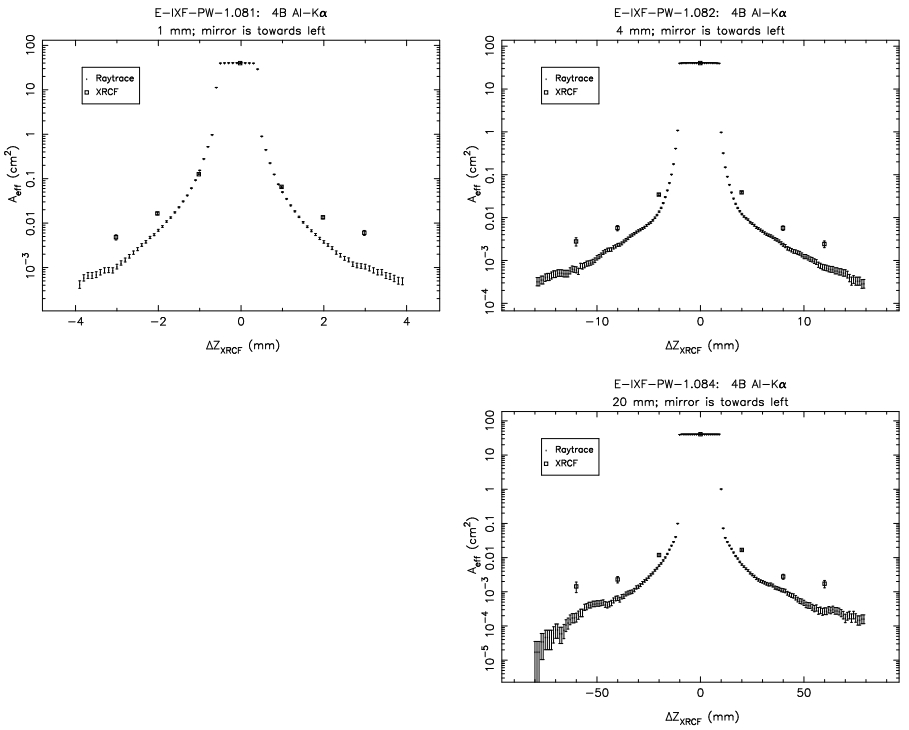

Figure 14.24: Pinhole effective areas; Shell 4B at Al-Kα.

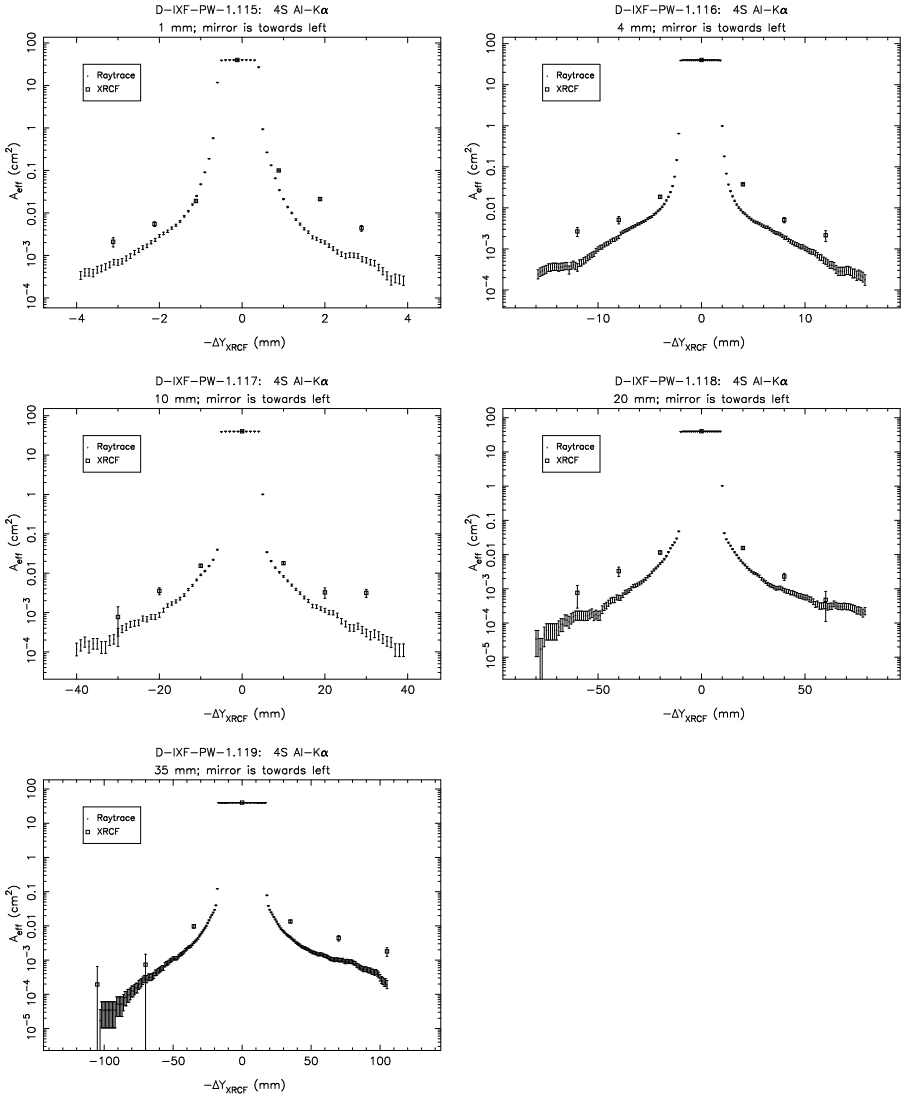

Figure 14.25: Pinhole effective areas; Shell 4S at Al-Kα.

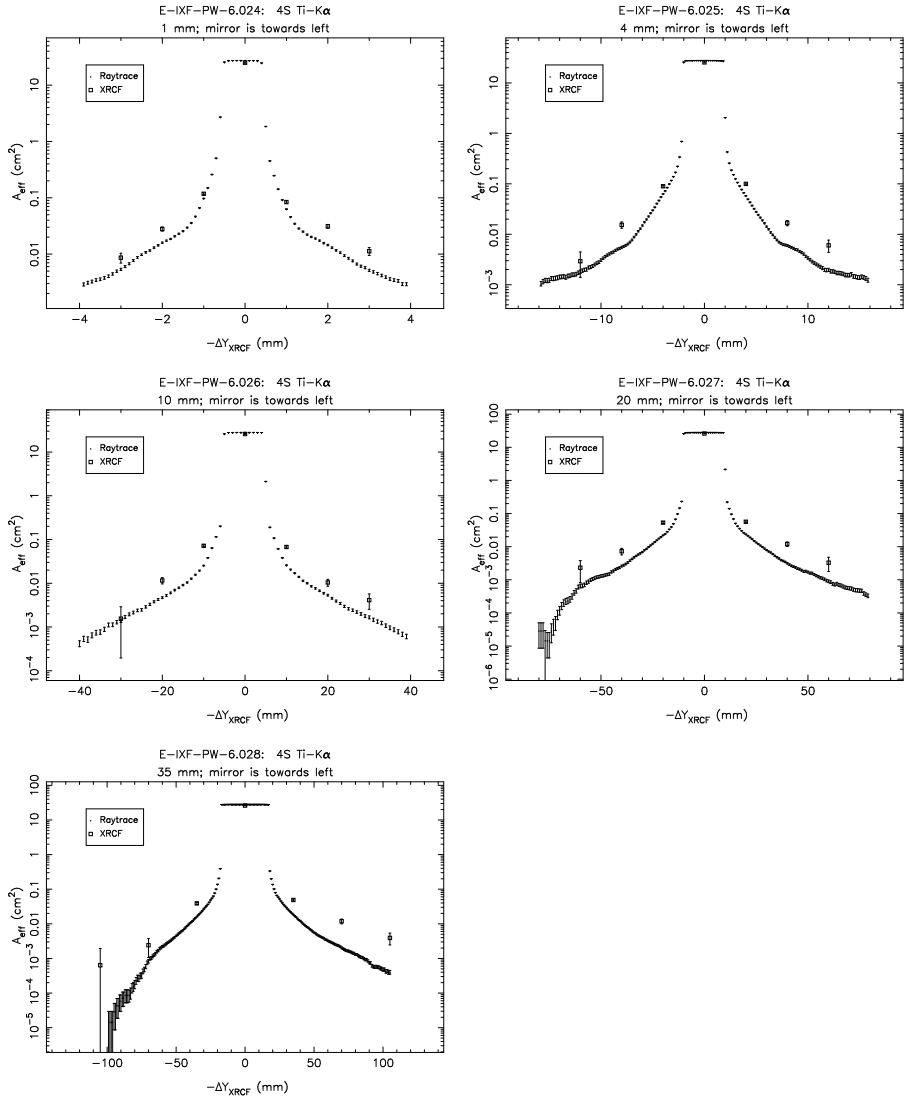

Figure 14.26: Pinhole effective areas; Shell 4S at Ti-Kα.

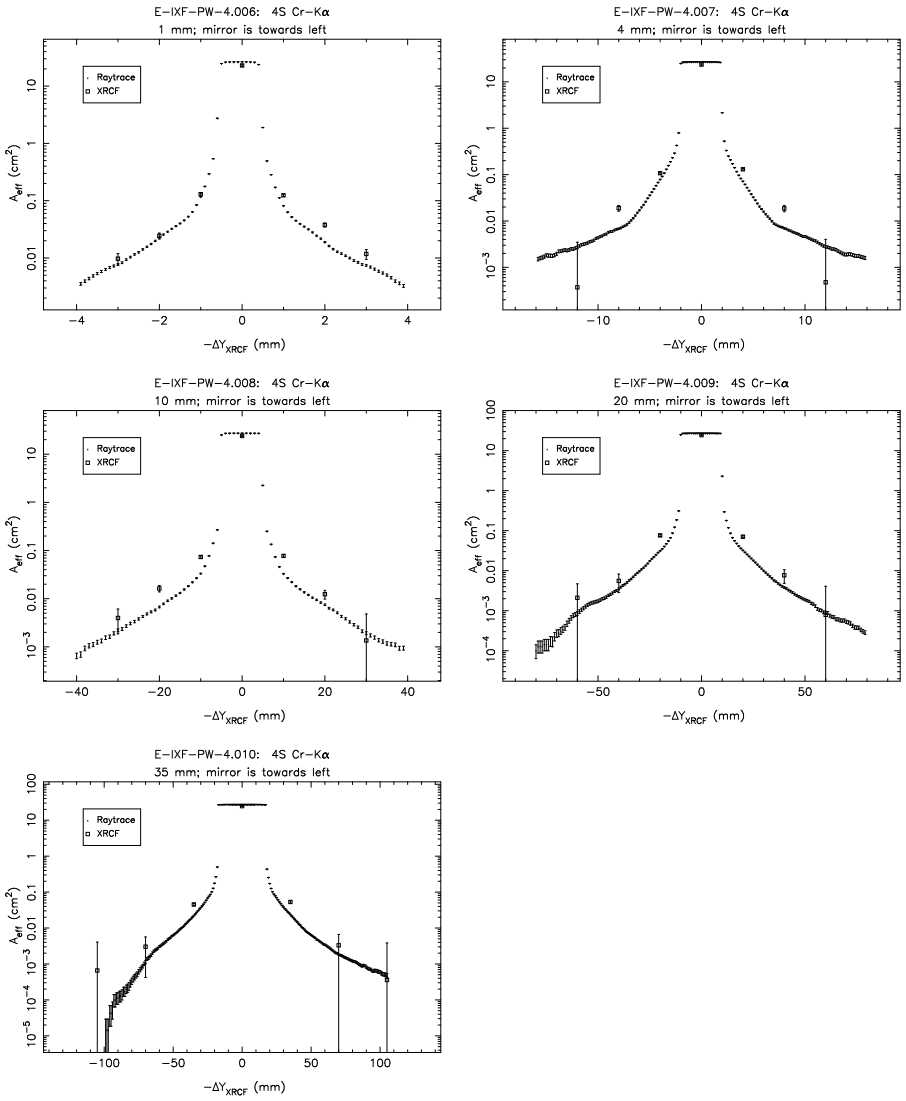

Figure 14.27: Pinhole effective areas; Shell 4S at Cr-Kα.

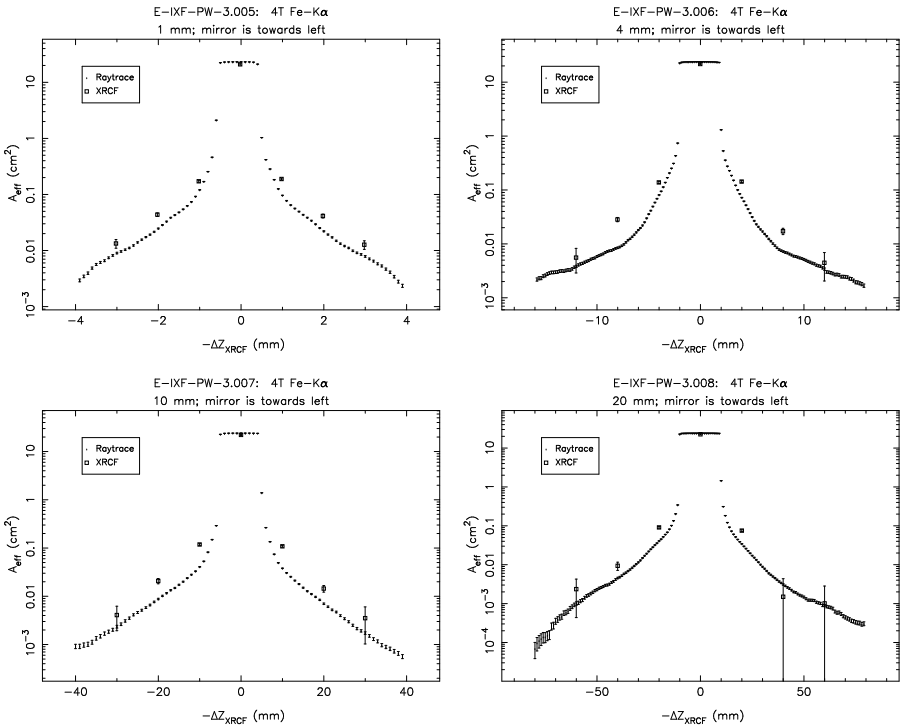

Figure 14.28: Pinhole effective areas; Shell 4T at Fe-Kα.

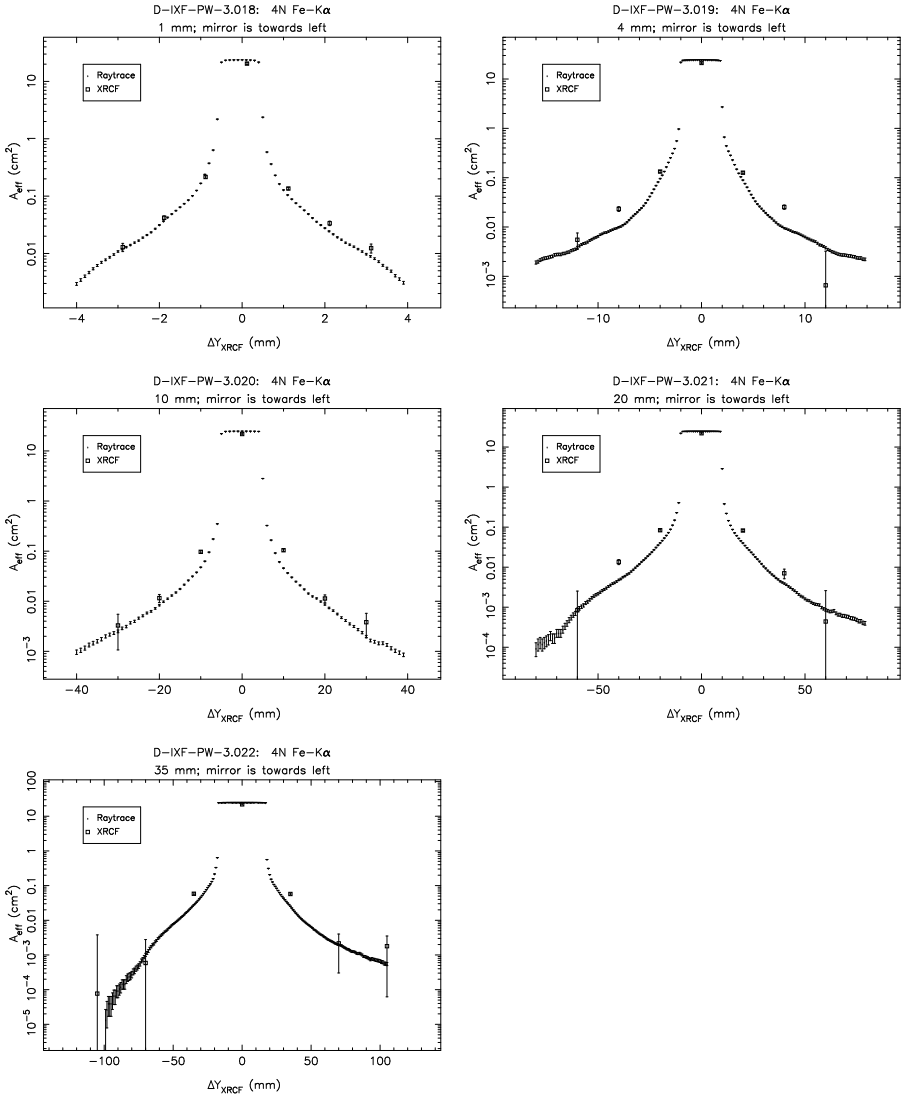

Figure 14.29: Pinhole effective areas; Shell 4N at Fe-Kα.

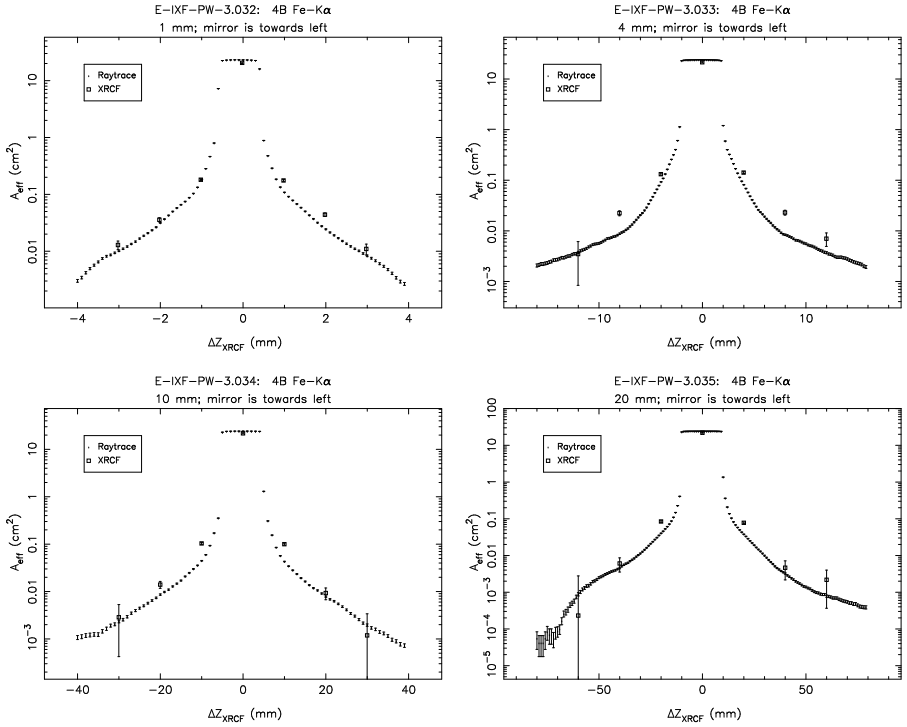

Figure 14.30: Pinhole effective areas; Shell 4B at Fe-Kα.

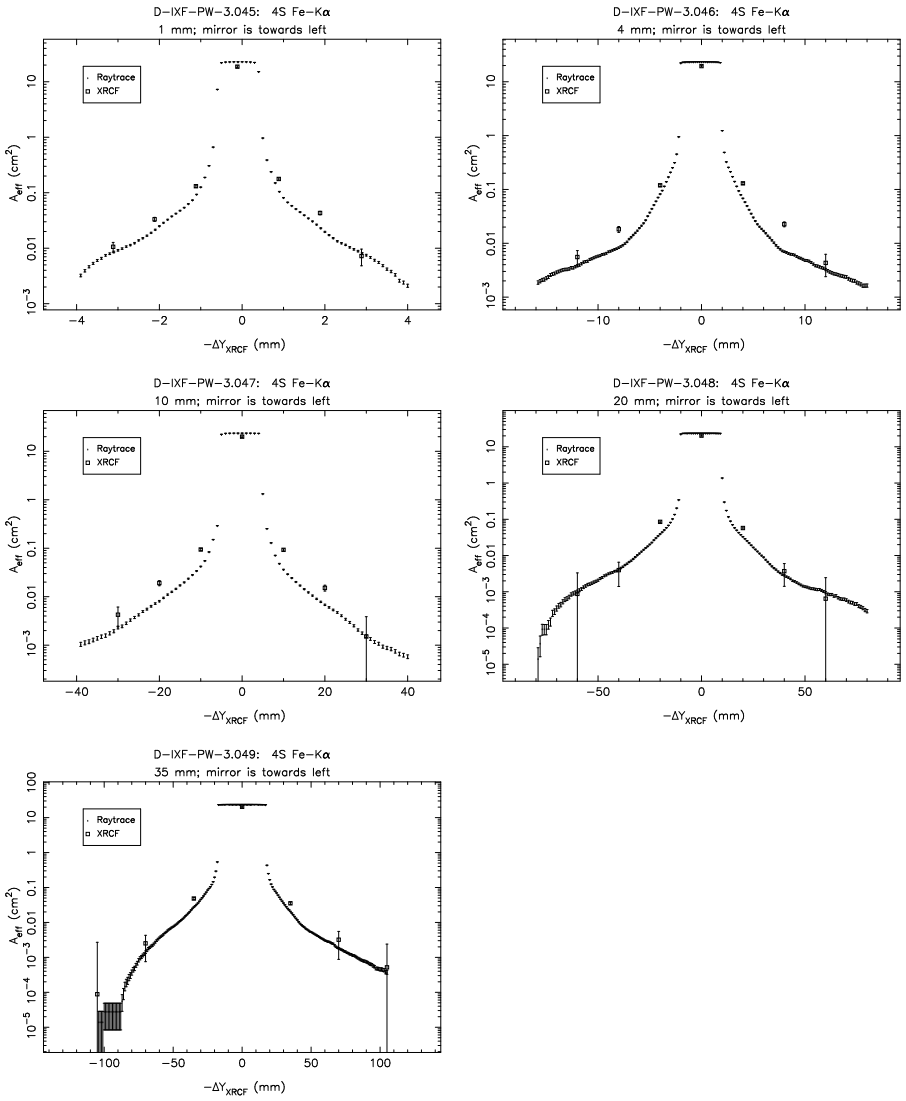

Figure 14.31: Pinhole effective areas; Shell 4S at Fe-Kα.

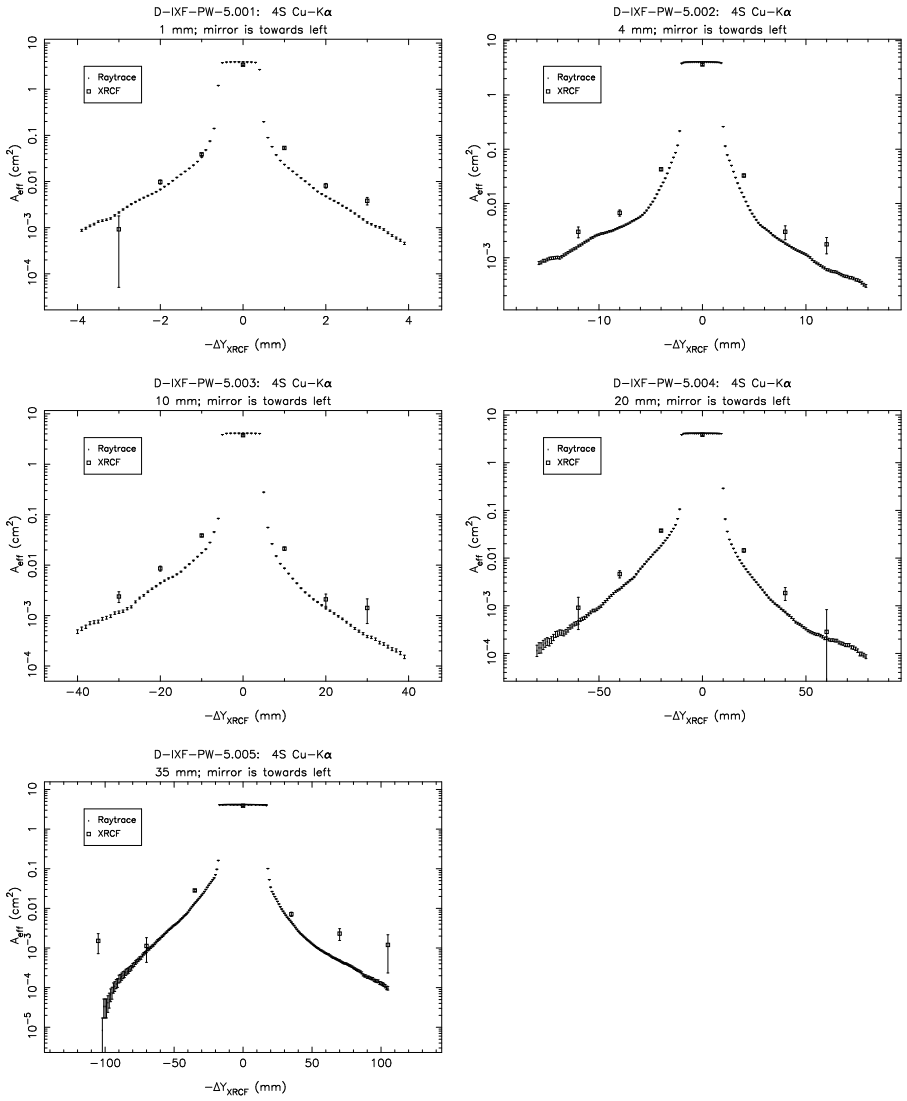

Figure 14.32: Pinhole effective areas; Shell 4S at Cu-Kα.

Shell 6 Single Quadrant Scans

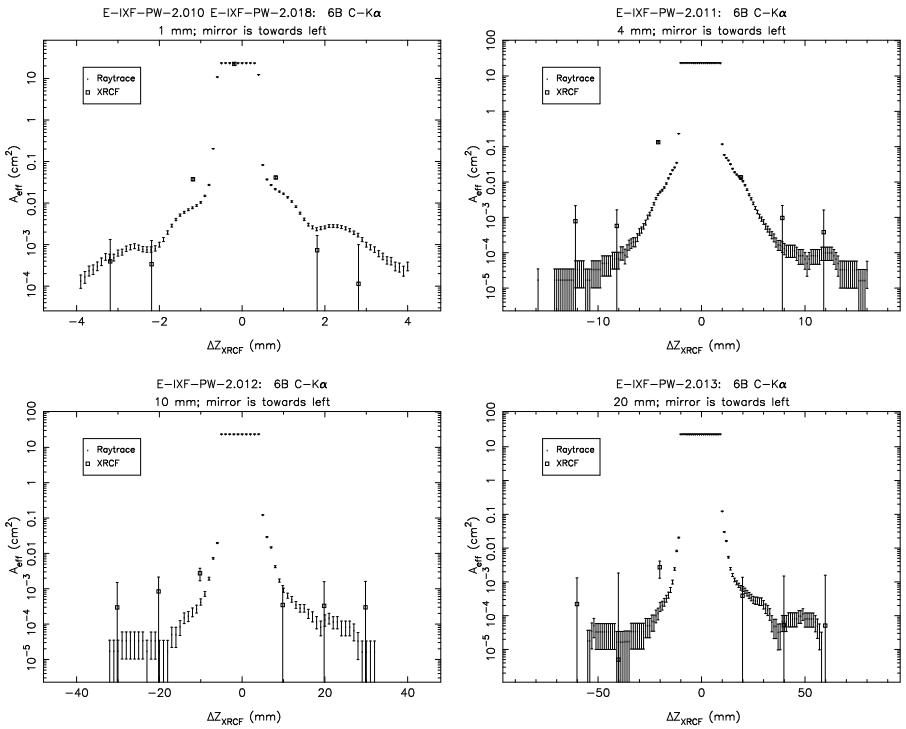

Figure 14.33: Pinhole effective areas; Shell 6B at C-Kα. The 4 mm pinhole effective area at $\Delta Z_{XRCF} = -4$ mm appears to be strongly discrepant; see §14.3.2.

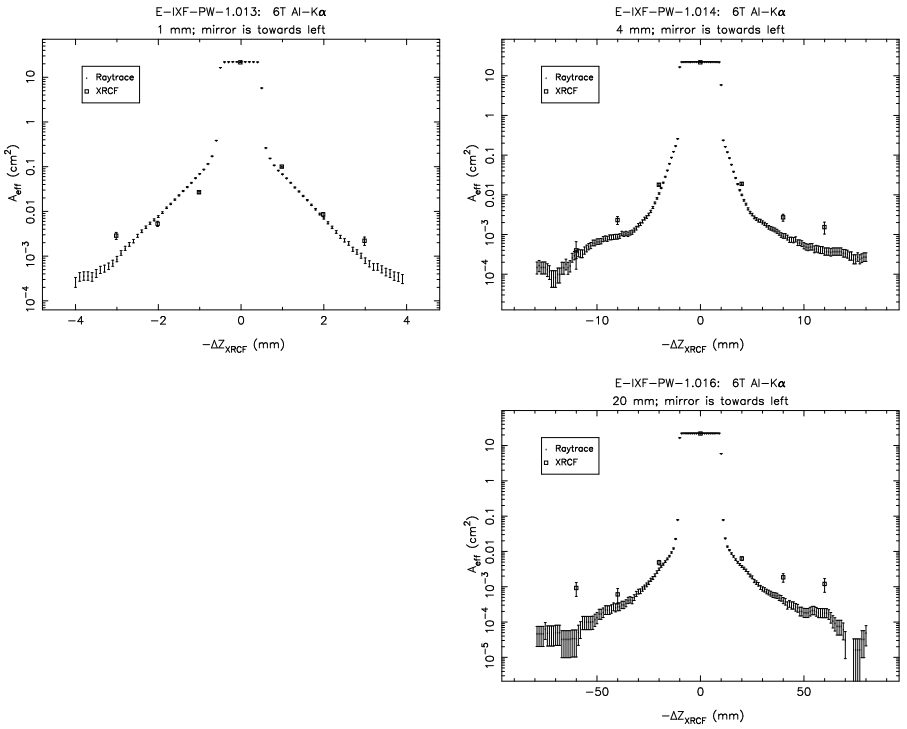

Figure 14.34: Pinhole effective areas; Shell 6T at Al-Kα.

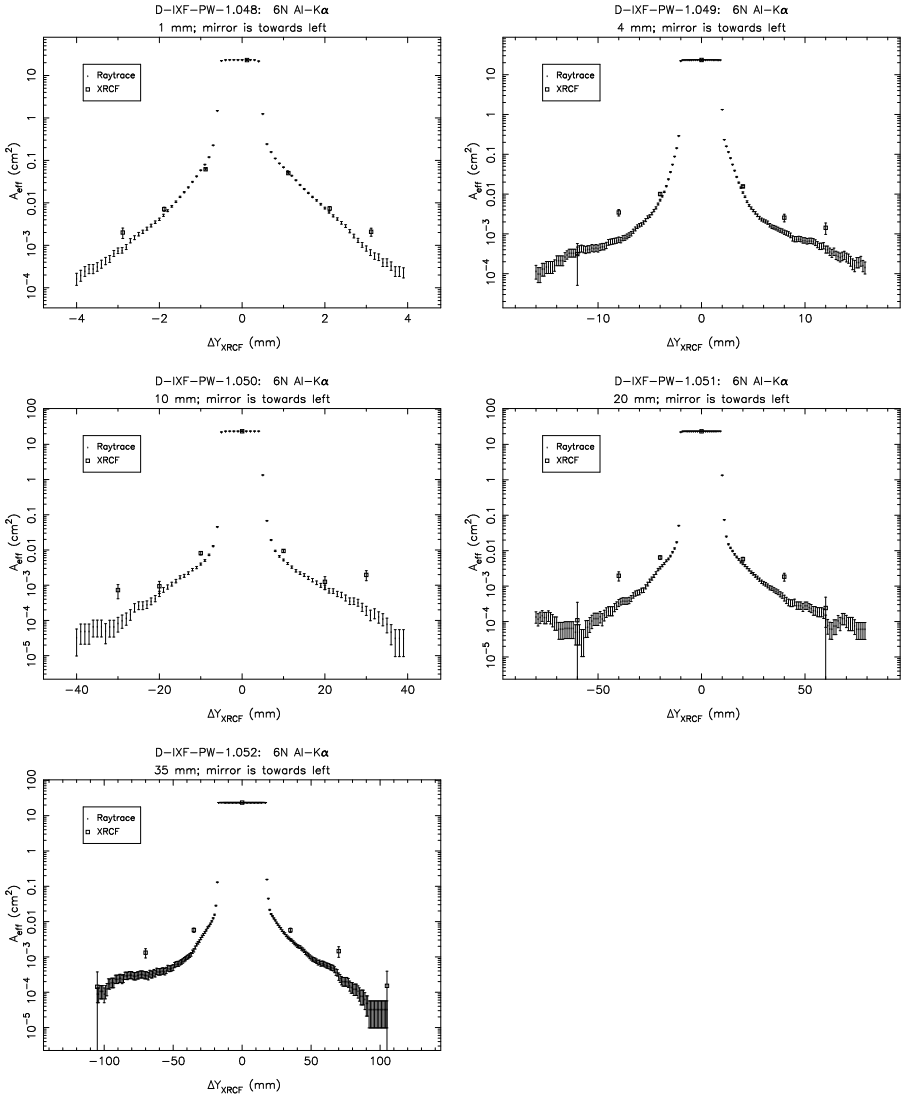

Figure 14.35: Pinhole effective areas; Shell 6N at Al-Kα.

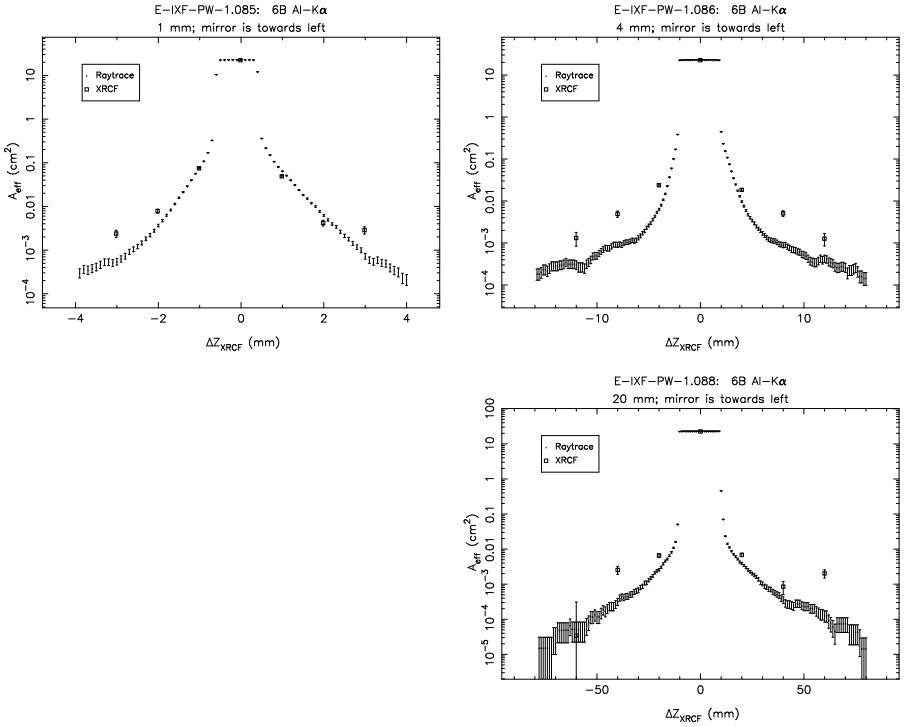

Figure 14.36: Pinhole effective areas; Shell 6B at Al-Kα.

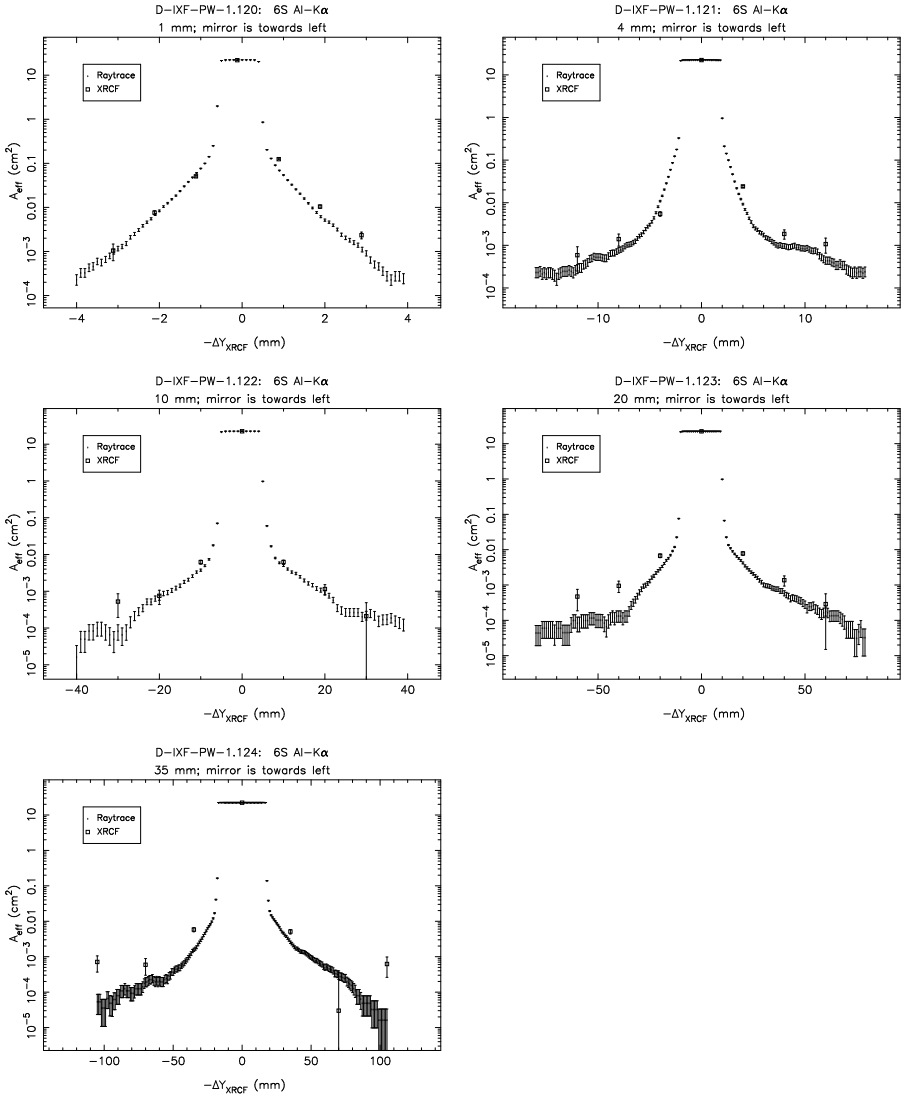

Figure 14.37: Pinhole effective areas; Shell 6S at Al-Kα.

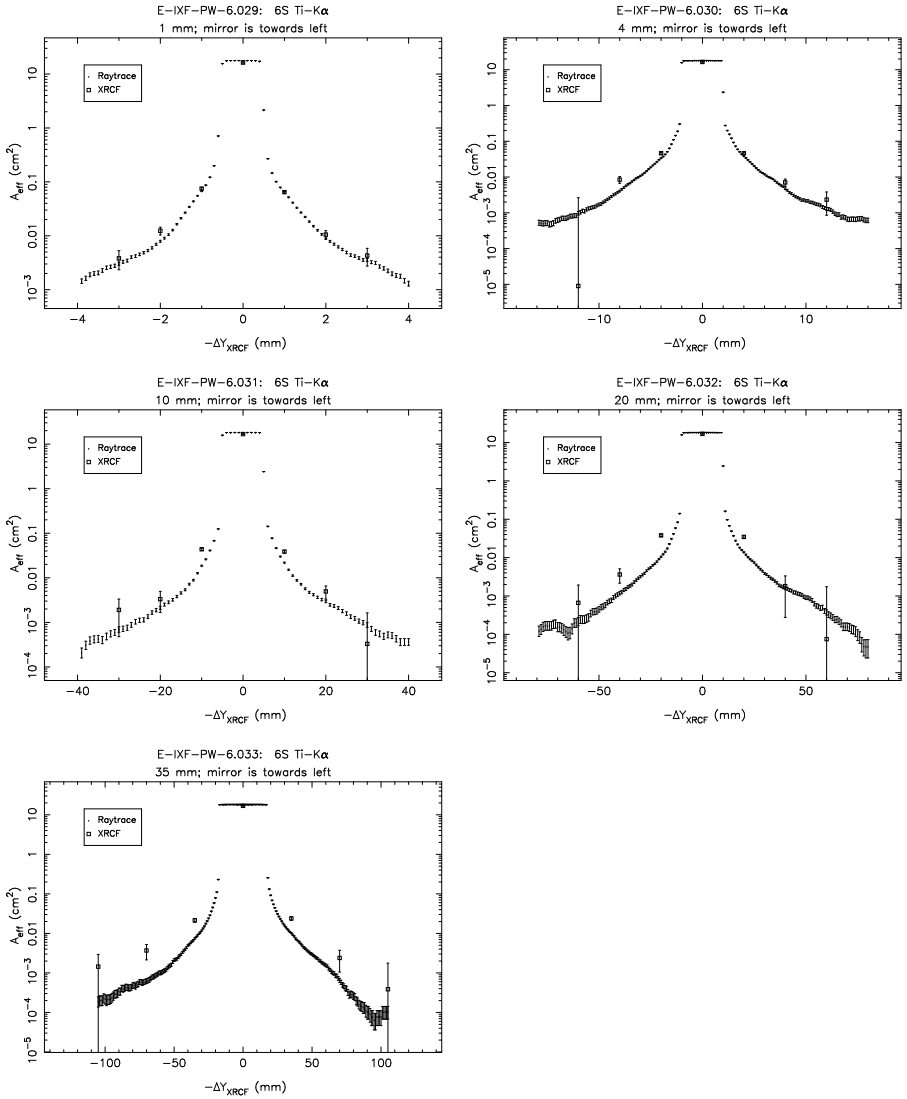

Figure 14.38: Pinhole effective areas; Shell 6S at Ti-Kα.

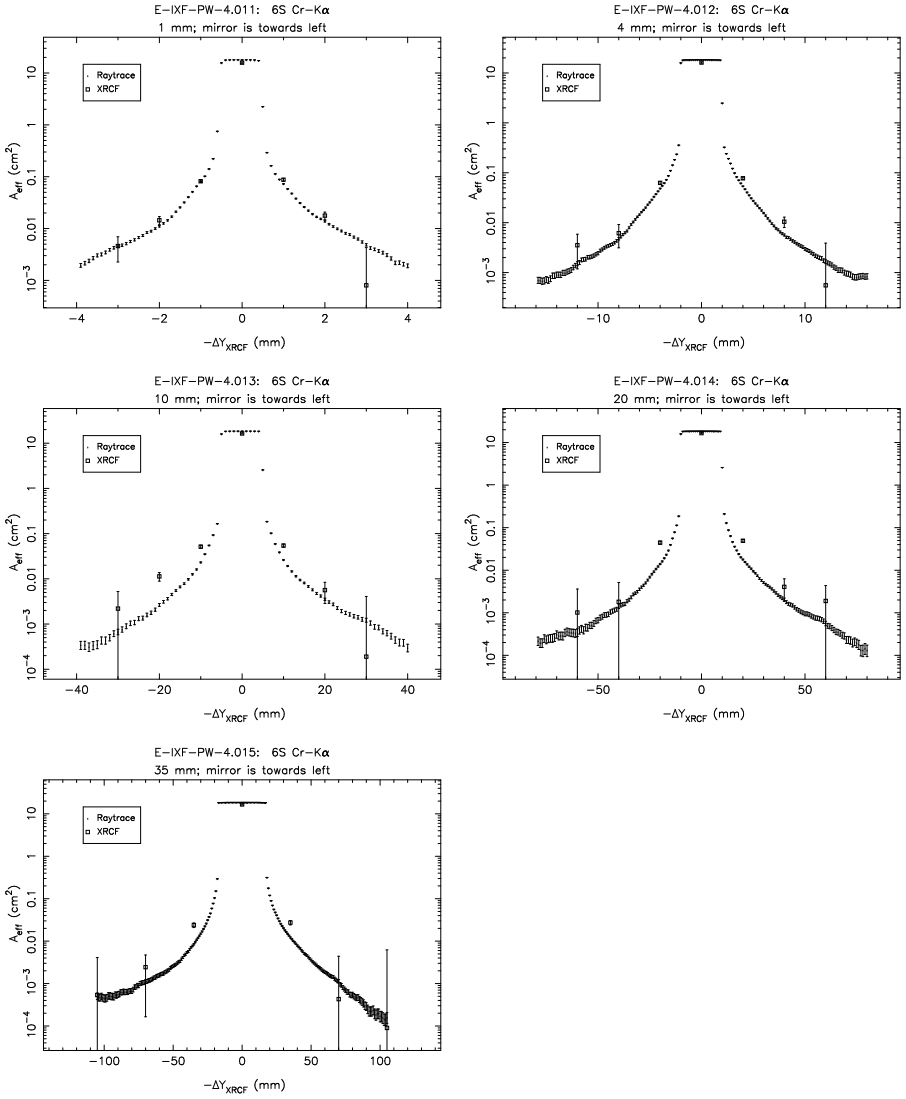

Figure 14.39: Pinhole effective areas; Shell 6S at Cr-Kα.

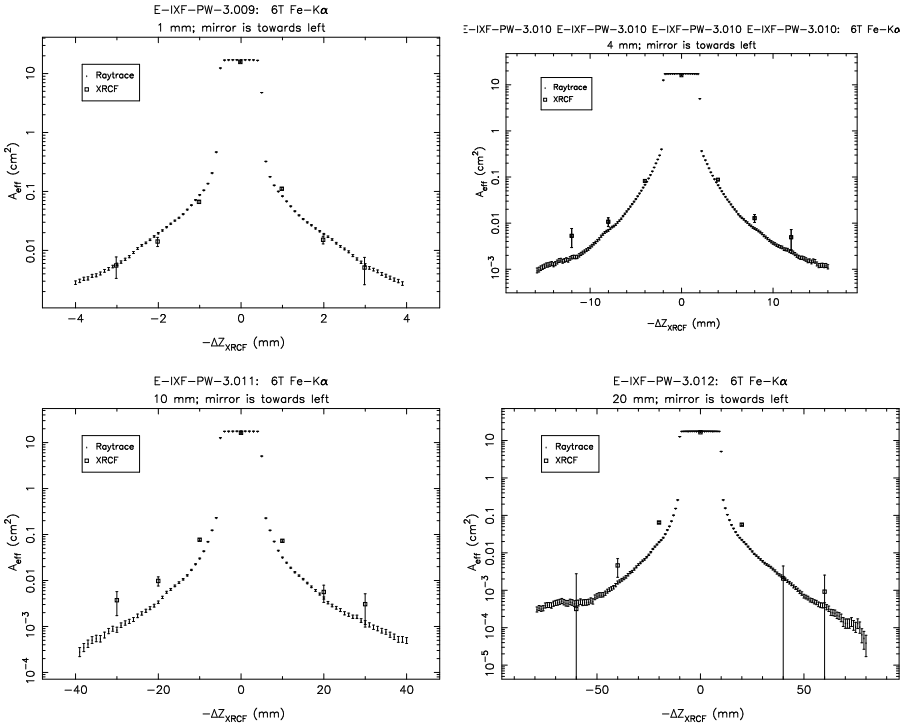

Figure 14.40: Pinhole effective areas; Shell 6T at Fe-Kα.

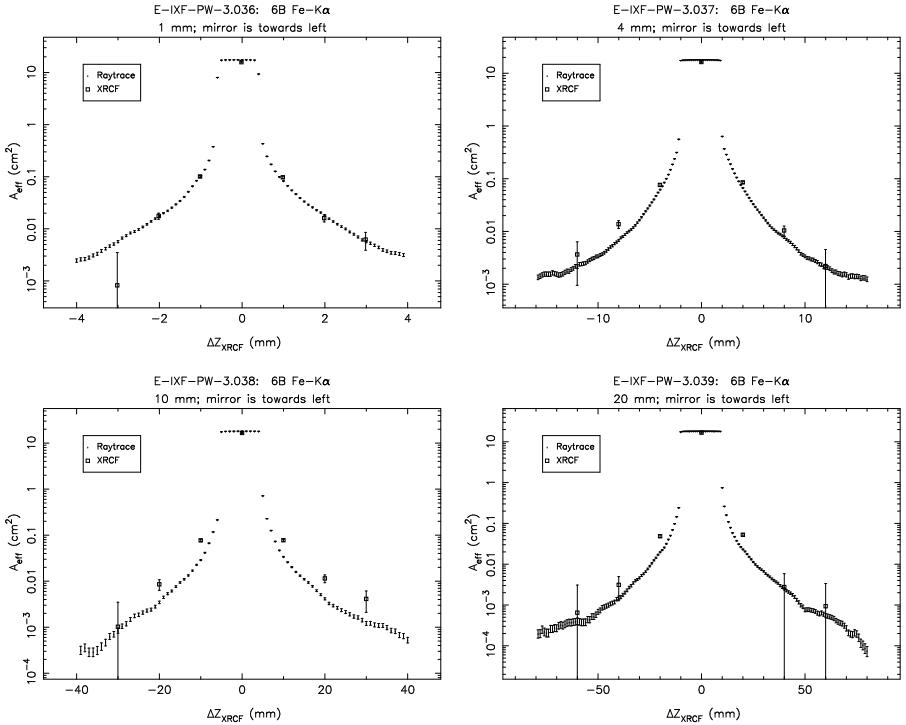

Figure 14.41: Pinhole effective areas; Shell 6B at Fe-Kα.

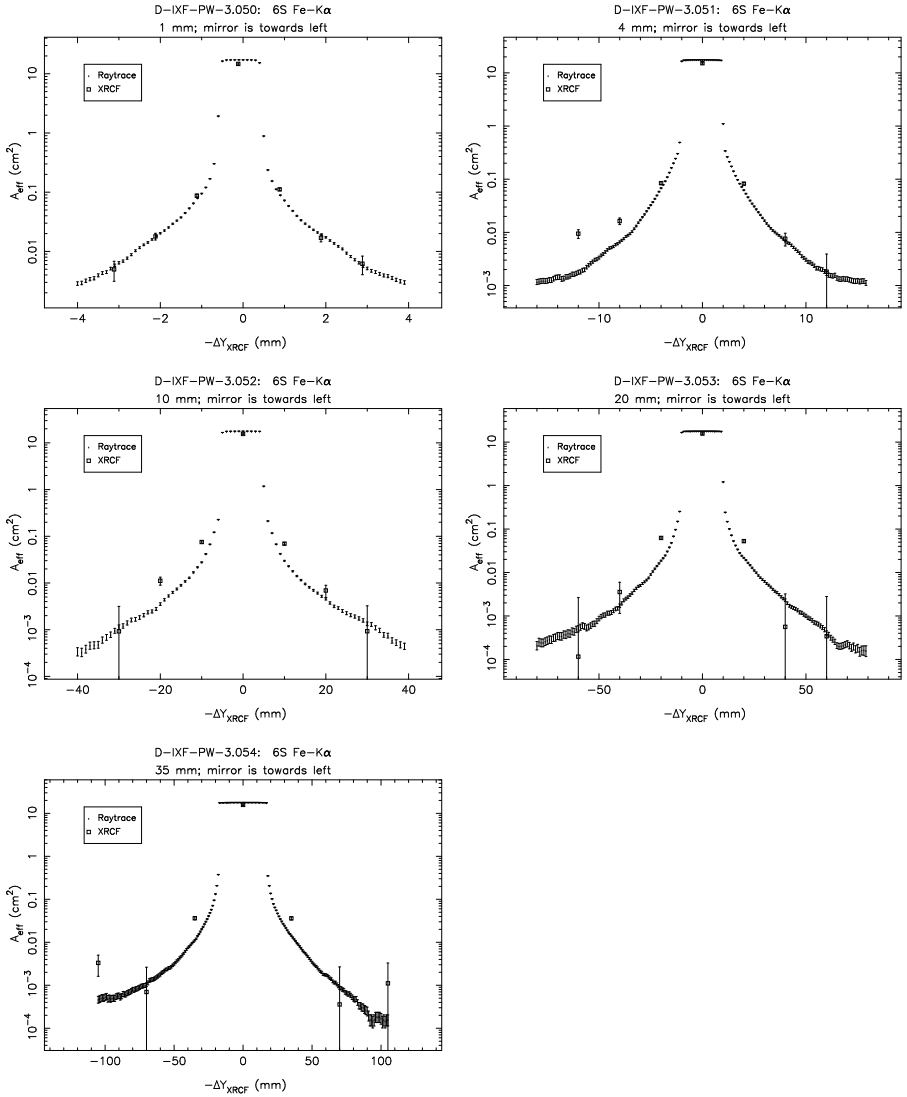

Figure 14.42: Pinhole effective areas; Shell 6S at Fe-Kα.

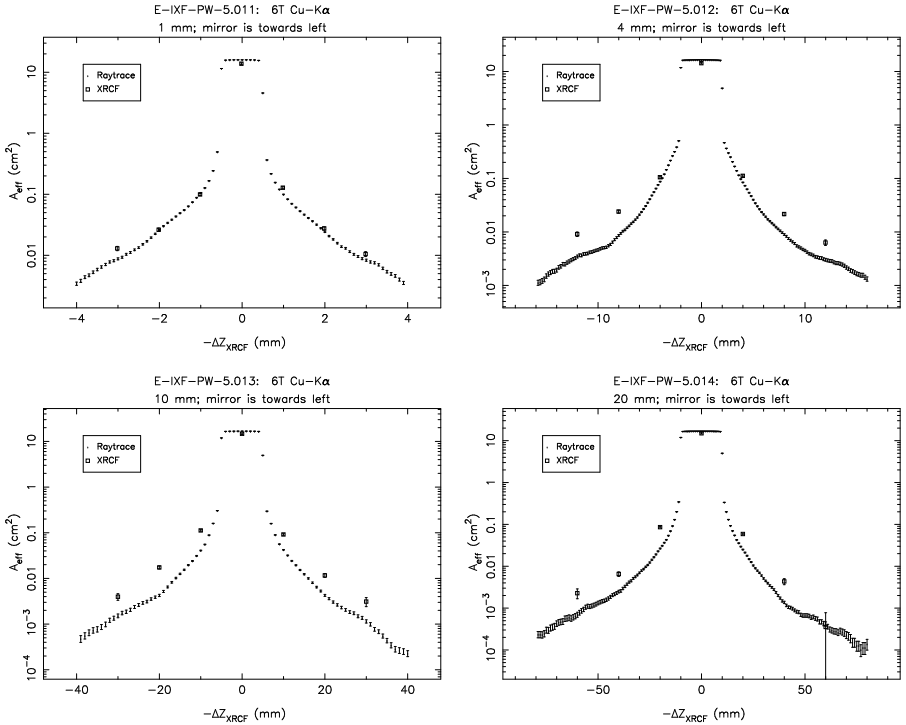

Figure 14.43: Pinhole effective areas; Shell 6T at Cu-Kα.

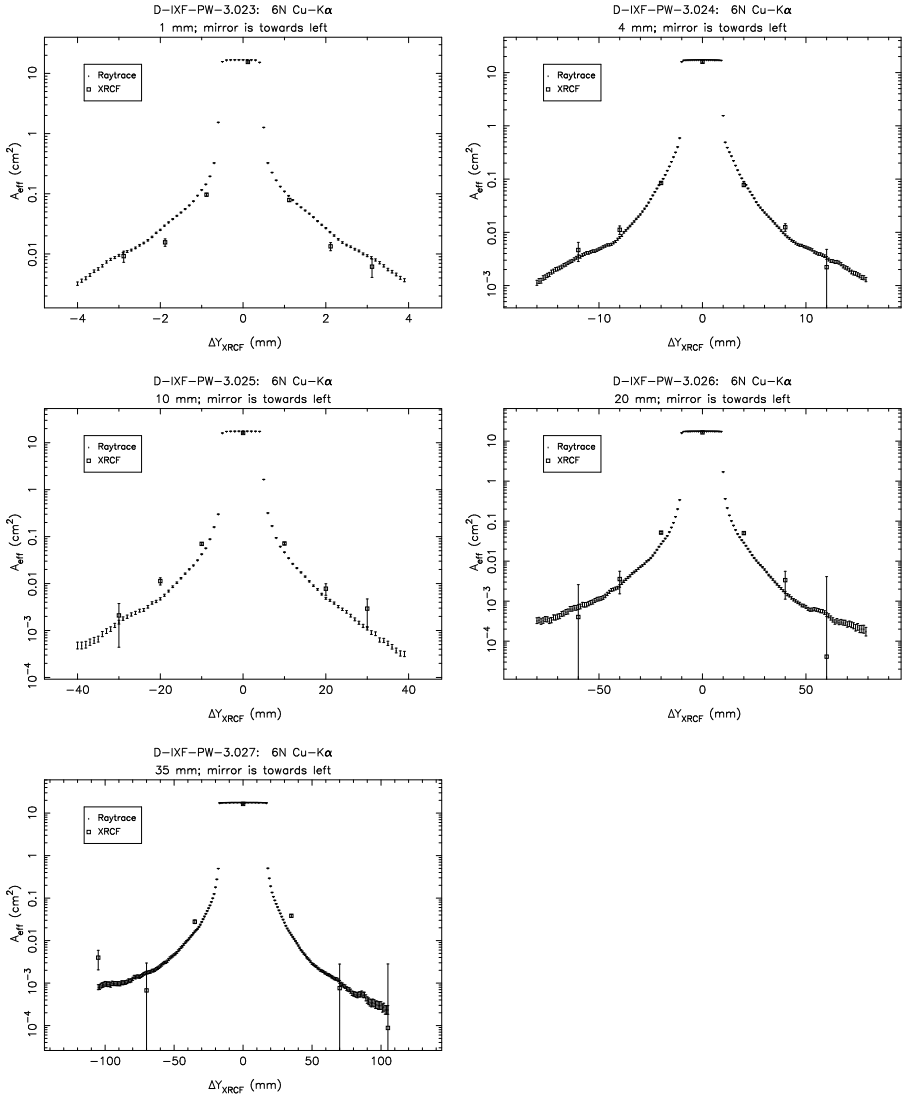

Figure 14.44: Pinhole effective areas; Shell 6N at Cu-Kα.

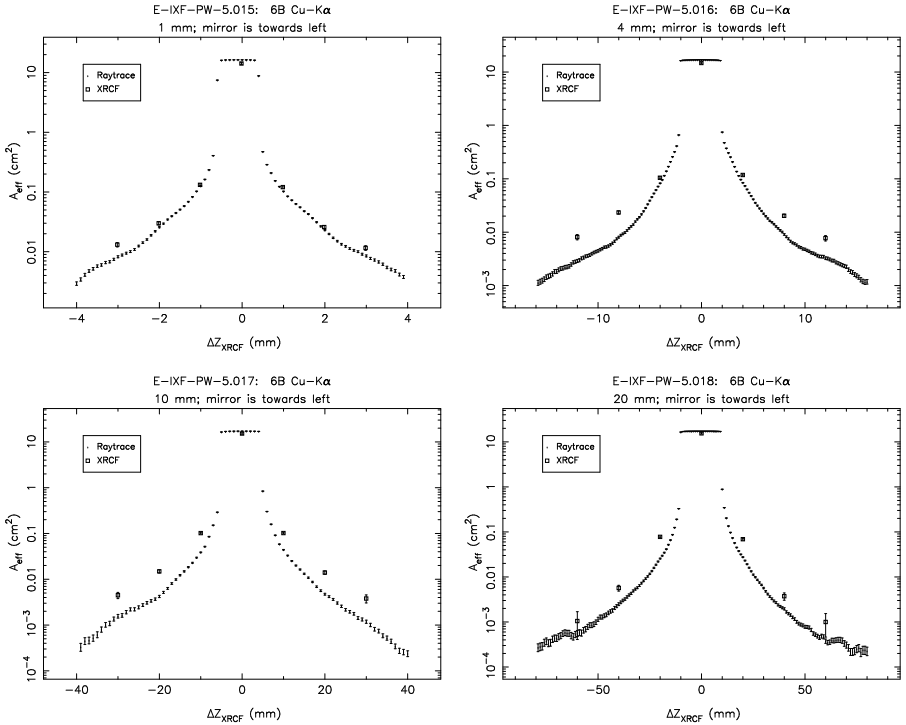

Figure 14.45: Pinhole effective areas; Shell 6B at Cu-Kα.

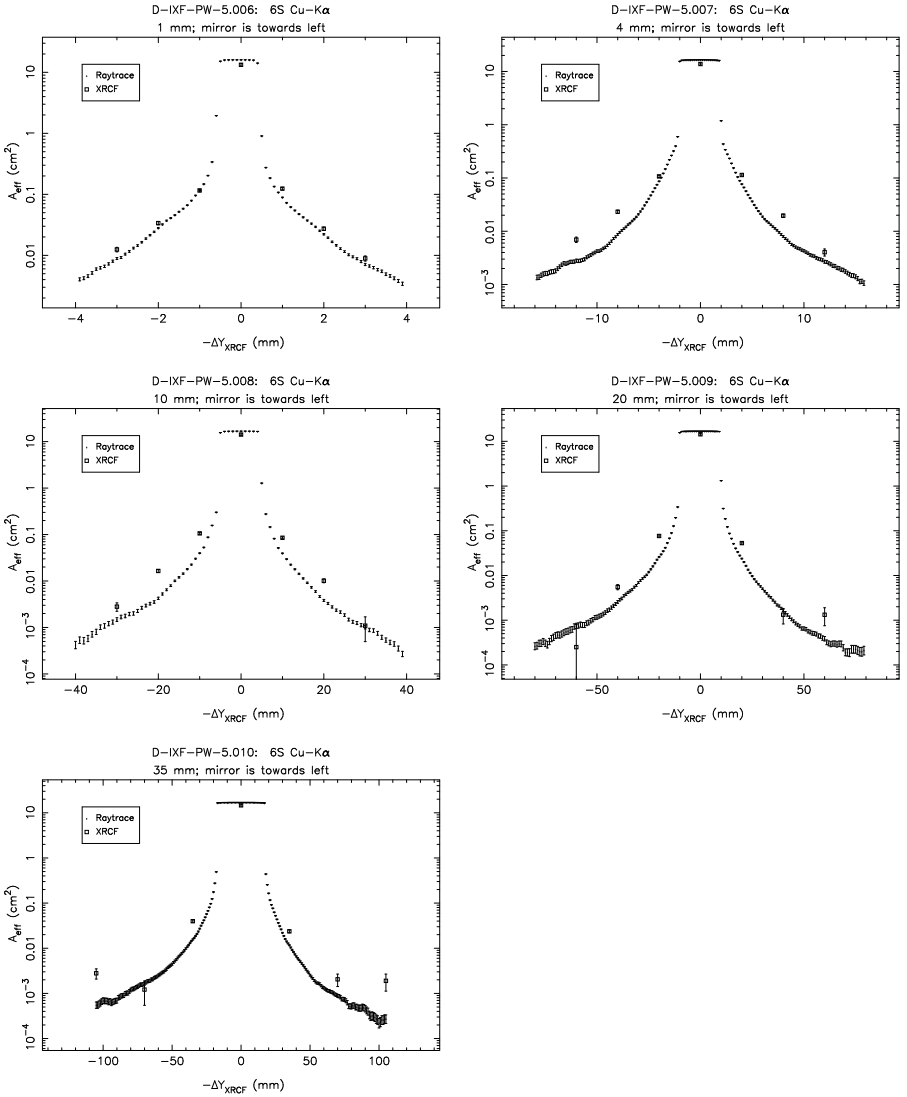

Figure 14.46: Pinhole effective areas; Shell 6S at Cu-Kα.

14.3.2 Transverse (out of plane) Wing Scan Pinhole Data

In this section the transverse pinhole scans at C-Kα are presented. A single set of "out-of-plane" scans was performed for quadrant 6B. These were in the Z direction rather than the Y direction; they may be compared to the normal "in-plane" scans in Figure 14.33.

The Y scans were performed with 1, 4, 10, 20, and 35 mm diameter pinholes. In the course of the 1 mm scans, it was discovered that the scan was approximately 500 μm too low. The reason for this is discussed in §D.7.1.

The FOA table was adjusted between the 1 mm and the 4 mm pinhole scan, so the 4, 10, 20, and 35 mm pinhole scans were at approximately the correct Z value. (It is believed that the data were taken approximately 100 μm too low, but this should not be a significant error; see §D.7.1.)

For the 1 mm pinhole raytrace simulation, the scan was along $Z = -0.6$ mm; the scan misses the core of the pinhole, resulting in a peaked distribution of pinhole effective area with pinhole position, rather than the flat-topped distribution more typically seen in the raytraces. Note also that in the raytraces, the handling of the out-of-plane scattering is simplistic: the out-of-plane scattering distribution is taken to be the in-plane scattering distribution scaled by the sine of the graze angle.

In examining the X-ray data for the 4 mm pinhole, it is notable that the pinhole effective area is definitely nonzero at -4 mm, but basically only an upper limit at $+4$ mm; see also the corresponding 6B C-Kα in-plane scan (Figure 14.33) conducted just after this scan. Again, examination of the raw data indicates that the difference is real and the available information on pinhole positions and tolerances indicate that these are accurate too. Unlike the in-plane case, in which the scattering distribution towards or away from the mirror is not necessarily symmetric about the peak, in this out-of-plane case, the expectation is that the situation should fully symmetric about the peak. The asymmetry in the 4 mm pinhole data is therefore puzzling. In both the in-plane and the out-of-plane cases for the 6B C-Kα scans, the 4 mm pinhole results are inconsistent with the 1 mm pinhole results based on relative pinhole areas. The 4 mm effective area at 4mm off-axis should be at most 16 times the 1 mm effective areas at 2 and 3 mm off-axis. Because we expect the surface brightness to be steeply falling, this should be a strong upper limit. Instead, the 4 mm effective area is a factor of 30 larger than the 1 mm effective areas for the out-of-plane case (Figure 14.47). In the case of the in-plane scan (Figure 14.33) the discrepency is even worse, with the 4 mm effective area more than a hundred times larger than can be accounted for by the 1 mm effective areas (even assuming a flat brightness distribution). Currently we have no explanation for these discrepencies.

Because of problems with shutters sticking, the 4N4S and 6N6S scans were performed with shutter 3B also open (*i.e.*, they were really 4N4S3B and 6N6S3B scans) In order to correct for this, additional 3B Z-scans at Al-Kα were performed for the 1 mm and 4 mm pinholes (see Figure 14.48); these provide an additional (albeit limited) sample of the out-of-plane wings. As noted in §14.3.3, the scan was only in one direction off-axis because of the presumed symmetry of the out-of-plane scattering.

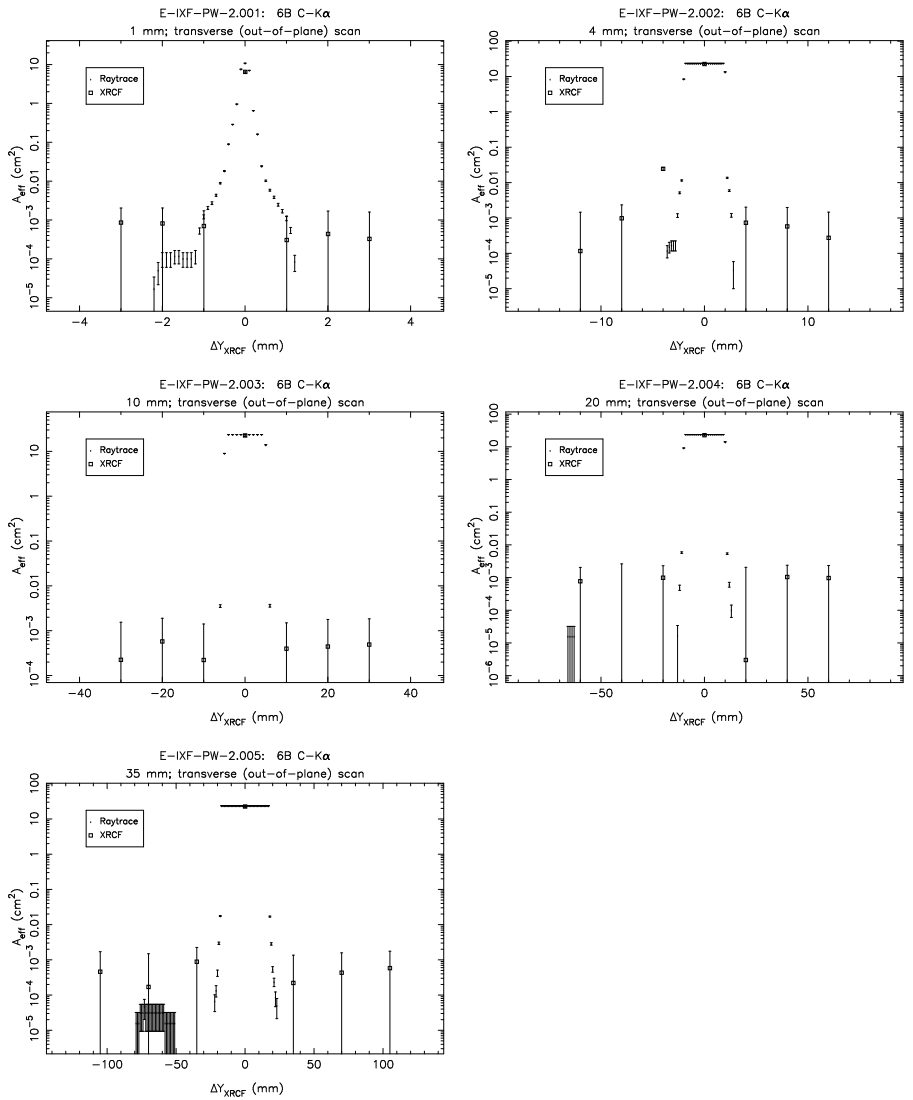

Figure 14.47: Pinhole effective areas; Shell 6B at C-Kα (*transverse scans*).

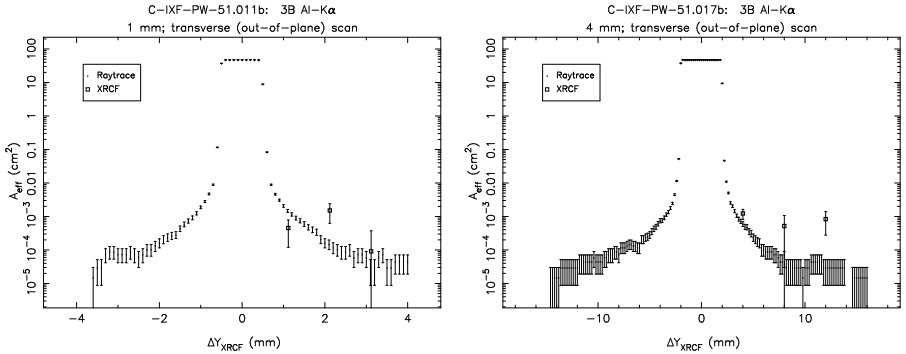

Figure 14.48: Pinhole effective areas. Left: 1 mm pinhole scan, Shell 3B at Al-Kα. Right: 4 mm pinhole scan, Shell 3B at Al-Kα. These 3B Y–scans were performed in order to correct the in-plane 4N4S and 6N6S scans which were made with the 3B shutter stuck open. (*transverse scans*).

14.3.3 Double Quadrant Wing Scan Pinhole Data

In this section the XRCF double quadrant wing scan pinhole effective area measurements are compared to the raytrace simulations of the same configurations. Unlike the single quadrant scans presented in §14.3.1, the HRMA was nominally at zero yaw and pitch. Because the profiles were expected to be symmetric, scans were performed only for points to one side ($+D_{ap}$, $+2D_{ap}$, and $+3D_{ap}$ for a given aperture diameter D_{ap}). Because of problems with shutters sticking, the 4N4S and 6N6S scans were performed with shutter 3B also open (*i.e.*, they were really 4N4S3B and 6N6S3B scans). In order to correct for this, additional 3B Z-scans at Al-Kα were performed for the 1 mm and 4 mm pinholes (see Figure 14.48).

Shell 4 Double Quadrant Scans

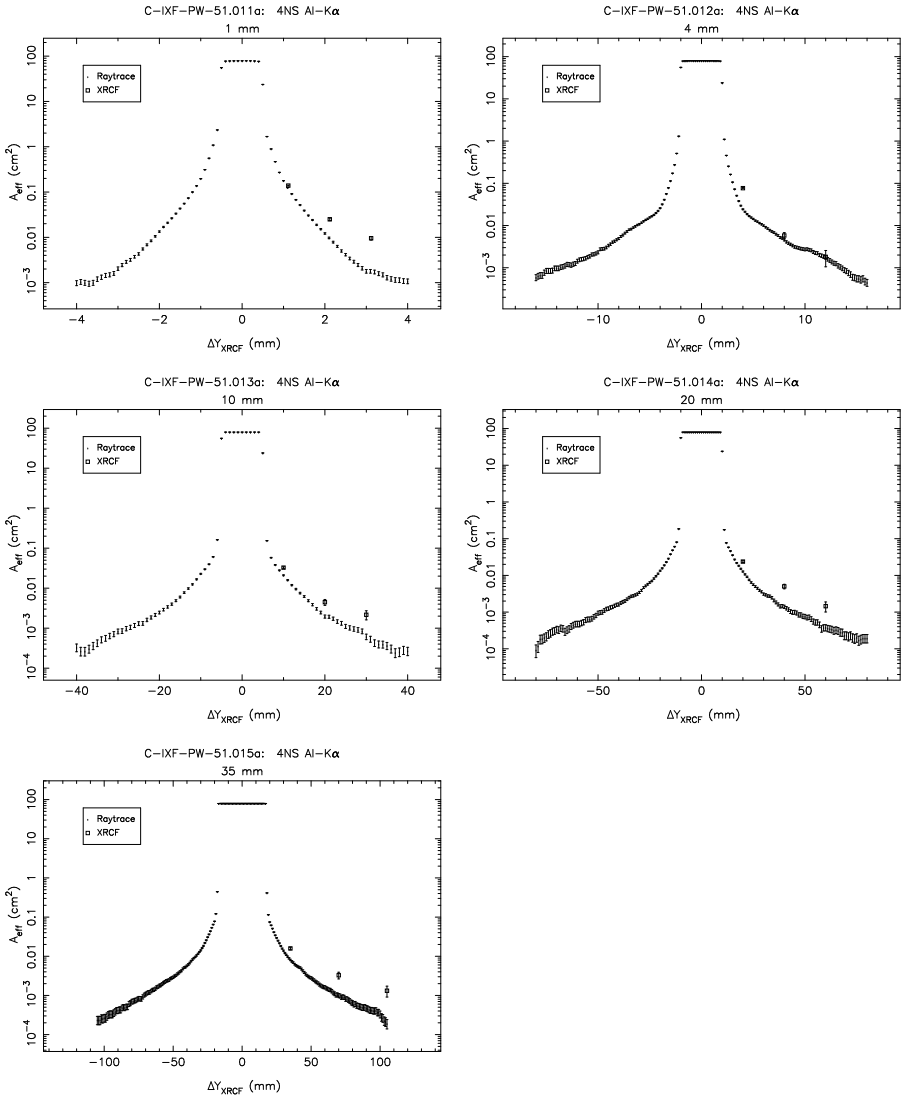

Figure 14.49: Pinhole effective areas; Shell 4NS at Al-Kα.

Shell 6 Double Quadrant Scans

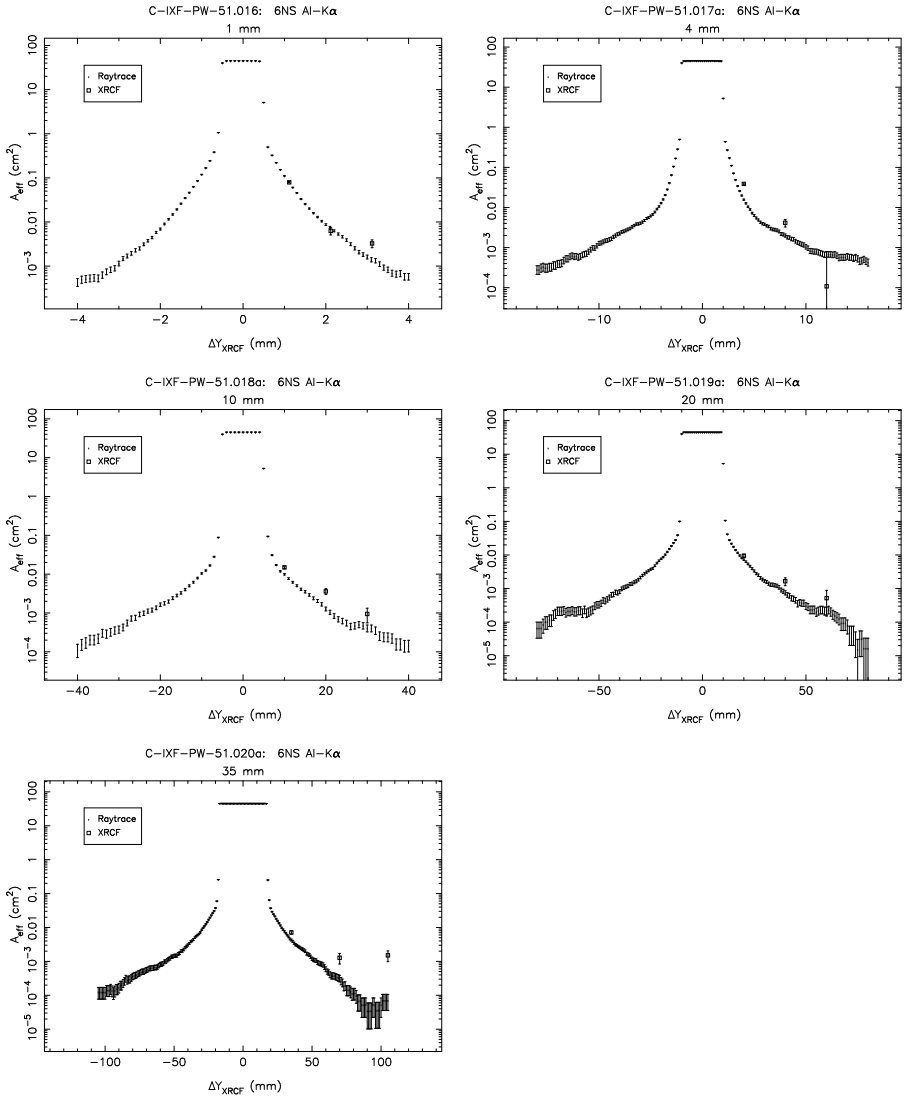

Figure 14.50: Pinhole effective areas; Shell 6NS at Al-Kα.

14.4 Discussion and Outstanding Issues

Other than for the effects of quadrant shutter vignetting, the raytrace data suggest that the pinhole effective area distribution is approximately symmetric. (Note, however, that the raytraces have a built-in symmetry in that the same scattering function is used for scattering both towards and away from the mirror surface; in reality, the distribution in the two directions is expected to be different.) For the most part, the X-ray data also show approximate symmetry. However, in a number of cases, the profiles appear to be markedly asymmetric: see 1S, 3T, 3N, 3B, 3T, 3S, 4S, 6T at Al-Kα. There seem to be no obvious trends. Based on the way the mirrors were manufactured, one would expect the same basic scattering properties for each quadrant, but at Al-Kα, while all four shell 3 quadrants show asymmetries in the 1 mm pinhole data, in shells 1, 4, and 6 only one quadrant shows such a marked asymmetry. Some part of the asymmetry may arise because of misalignment of the pinhole scan to the core of the image, particularly for the innermost points which are on a steeply falling portion of the wings. In a case like the 3T Al-Kα 1 mm pinhole data, this does not appear plausible, though.

A peculiar case is that of the 6B C-Kα in-plane scans (Figure 14.33) and out-of-plane scans (§14.3.2). In both cases, the 4 mm pinhole scans show large asymmetries between the effective areas for pinholes 4 mm to either side of the core. This is particularly puzzling in the case of the out-of-plane scan in which the the symmetry of the experiment leads one to expect a symmetric distribution. In contrast to the 4 mm pinhole data, the 1 mm pinholes do not show strong evidence for the asymmetry. Any pinhole positional errors large enough to reconcile the data (of order 1 or 2 mm) are improbably large compared to the known tolerances on pinhole positioning, and errors of this magnitude (arising, say, from an incorrect value in the FOA table) would have been detected in other experiments using smaller pinholes. Furthermore, the effective area found for the 4 mm pinhole position 4 mm off-axis is *strongly inconsistent* with the 1 mm pinhole measurements at 2 and 3 mm off-axis. Currently we have no explanation for these anomalies in the 6B C-Kα pinhole scan 4 mm pinhole effective areas.

14.5 Raytrace and Data Reduction Versions

The data reductions described in this chapter used the following software versions:

```
FitAll2 script:             1.12 $Date: 1998/06/11 13:55:25 $
calcstage4 script:          1.7 1998/04/16 18:55:00
Wingscan script:            1.6 1998/05/14 18:23:07
```

The raytrace simulations described in this chapter used the following software versions:

```
raytrace script:            trace-shell5
raytrace configuration:     xrcf_SA01G+HDOS_HDOS-scat-980623_01.cnf
quadrant shutter script:    quad_shutter_05.lua
```

The raytraces used for evaluating the mesh correction (Table 14.4) also include updated optical constants, and a "modified Debye-Waller" treatment of the effects of interface gradients in the multilayer stack. These raytraces used the following software:

```
raytrace script:            trace-xrcf1
raytrace configuration:     xrcf_xss_05.cnf
quadrant shutter script:    quad_shutter_05.lua
mesh module:                D951201
```